SYNTHESIS, CHARACTERIZATION AND PHOTOCATALYTIC APPLICATION OF NANOSTRUCTURED TUNGSTEN OXIDE / GRAPHENE NANOCOMPOSITES

BY

MOHAMAD OMAR ALFAWAKHIRY

A Thesis Presented to the

DEANSHIP OF GRADUATE STUDIES

KING FAHD UNIVERSITY OF PETROLEUM & MINERALS

DHAHRAN, SAUDI ARABIA

In Partial Fulfillment of the
Requirements for the Degree of

MASTER OF SCIENCE

In

CHEMISTRY

NOVEMBER 2014

KING FAHD UNIVERSITY OF PETROLEUM & MINERALS

DHAHRAN- 31261, SAUDI ARABIA

DEANSHIP OF GRADUATE STUDIES

This thesis, written by Mohamad Omar Alfawakhiry under the direction of his thesis advisor and approved by his thesis committee, has been presented and accepted by the Dean of Graduate Studies, in partial fulfillment of the requirements for the degree of **MASTER OF SCIENCE IN CHEMISTRY.**

Dr. Tawfik A. Saleh
(Advisor)

Dr. Abdulaziz A. Al-Saadi
Department Chairman

Dr. Abdulaziz A. Al-Saadi

(Member)

Dr. Salam A. Zummo
Dean of Graduate Studies

Dr. Mohammad Qamar
(Member)

8/12/14

Date

Dedicated to
My
Family and friends

ACKNOWLEDGMENTS

All praise and glory be to Allah almighty for his assistance and supervision to complete this work. Thereafter, acknowledgment is due to King Fahd University Of Petroleum and Minerals where I had the chance to pursue my master studies.

I would like to express my gratitude and appreciation to my supervisor Dr. *Tawfik Saleh* for his efforts and continuous support with me and I am very thankful and grateful to my thesis committee members Dr. *Abdulaziz Al-Saadi* and Dr. *Mohammad Qamar* for their valuable suggestions and limitless help.

My deep acknowledgment goes to all faculty members of chemistry department and also to all members of center of excellence in nanotechnology and particularly the Director *Dr. Zain Yamani* for his support and help.

My gratitude goes to all my friends especially Wasim, Ghiath, Wael, Mohee Aldeen, Tamim, Firas and Jabari. Last, but certainly not least, my most sincere thanks go to my great parents and siblings and to my wife for their standing with me to complete this humble work.

TABLE OF CONTENTS

LIST OF TABLES

LIST OF FIGURES

LIST OF ABBREVIATIONS

MOS	:	Metal oxide semiconductor
BA	:	Benzyl alcohol
MBA	:	4-methoxy benzyl alcohol
CA	:	Cinnamyl alcohol
Gn	:	Graphene
Go	:	Graphene oxide
Gt	:	Graphite
GC-MS	:	Gas chromatography- mass spectroscopy
FESEM	:	Field emission scanning electron microscopy
XRD	:	X ray diffraction
BET	:	Brauner-Emmet-Teller **(**Surface Area & Porosity Analysis)
EDS	:	Energy dispersive X-ray spectroscopy
TEM	:	Transmission electron microscopy
WO_3-A	:	prepared in the presence of hydrochloric acid
WO_3-B	:	prepared in the presence of oxalic acid
WO_3-C	:	prepared in the presence of oxalic acid and hydrochloric acid

ABSTRACT

Full Name : Mohamad Omar Alfawakhiry

Thesis Title : Synthesis, characterization and photocatalytic application of nanostructured tungsten oxide/graphene nanocomposites

Major Field : Chemistry

Date of Degree : 2014

This research studies different types of hydrothermally synthesized nanostructured tungsten oxide and the effect of the presence of oxalic acid and hydrochloric acid on the morphology and the nanosize of the synthesized crystals. The work contains three nanocomposites of tungsten oxide including deposition of platinum nanoparticles (Pt/WO_3), tungsten oxide - graphene nanocomposite (WO_3/graphene) and platinum nanoparticles- tungsten oxide - graphene nanocomposite (Pt/WO_3/graphene). The work includes examination of parameters such as the best concentrations, ratios and conditions for the heterogeneous photocatalytic oxidation of benzyl alcohol, 4-methoxy benzyl alcohol and cinnamyl alcohol in aqueous suspensions at ambient conditions under simulated sunlight. The work includes nanostructured tungsten oxide characterization by means of field emission scanning electron microscope, X-ray diffractometer, Surface Area & Porosity Analyzer, Nano/Micro Particles Analyzer, X-ray photoelectron spectrometer and UV-Vis spectroscope. The presence of platinum nanoparticles on tungsten oxide surface was characterized by transmission electron microscope, Graphene nanocomposite characterization was conducted by field emission scanning electron microscope, Raman spectrometer and Fourier transform infrared spectroscope. The results show that the photocatalytic activity of nanostructured tungsten oxide differs with the morphology and the crystals size. Also shows high improvement in photocatalytic activity was observed by deposition of platinum with high conversion and selectivity, and even higher conversion using Pt/WO_3/graphene.

ملخص الرسالة

الاسم الكامل: محمد عمر الفواخيري

عنوان الرسالة: تصنيع وتوصيف وتطبيق تحفيز ضوئي للمركبات النانوية أوكسيد التنغستين النانوي \ الغرافين

التخصص: كيمياء

تاريخ الدرجة العلمية: سبتمبر 2014

تبحث هذه الدراسة أنواعا مختلفة من اوكسيد التنغستين النانوي المصنعة حرارمائياً وتأثير وجود حمض الأوكساليك وحمض كلور الماء على البنية والحجم النانوي للبلورات المصنعة, وتحتوي الدراسة ثلاثة مركبات نانوية لأوكسيد التنغستين هي البلاتين النانوي المرسب على سطح اوكسيد التنغستين (Pt/WO_3) والمركب النانوي اوكسيد التنغستين – غرافين (WO_3/graphene) و المركب النانوي بلاتين – اوكسيد التنغستين – غرافين (Pt/WO_3/graphene) وتتضمن الدراسة أختبار أفضل التراكيز والنسب والعوامل للأكسدة الحفزية الضوئية اللامتجانسة للبنزيل الكحول و 4- ميثوكسي بنزيل الكحول و سينياميل الكحول في المعلقات المائية في الظروف العادية وباستعمال ضوء محاكي لضوء الشمس ,وتشمل هذه الدراسة توصيفا لأوكسيد التنغستين النانوي بواسطة المجهر الالكتروني الماسح للانبعاثات الحقلية , مقياس حيود اشعة أكس ,محلل السطح النوعي والمسامية , محلل حجم الجزيئات الماكروية والنانوية , مطياف الالكترونات المثارة بالاشعة السينية (XPS) و مطيافية الاشعة المرئية وفوق البنفسجية. وتشمل توصيفاً لوجود البلاتين النانوي على سطح اوكسيد التنغستين بواسطة المجهر الإلكتروني النافذ والمركبات النانوية الحاوية على الغرافين بواسطة المجهر الالكتروني الماسح للانبعاثات الحقلية , مطياف رامان ,مطياف الاشعة تحت الحمراء, وتظهر الدراسة ان الفعالية الضوئية الحفزية لأكسيد التنغستين النانوي تختلف باختلاف البنى البلورية والحجم النانوي وأن الفعالية الضوئية الحفزية تتحسن بشكل كبير عند وجود البلاتين في (Pt/WO_3) وبشكل اكبر لدى استعمال (Pt/WO_3/graphene).

CHAPTER 1

INTRODUCTION

1.1 Semiconductors for photocatalysis

Due to their properties including the electrical, surface area, band gap energy, and optical properties, semiconductors have gained the attention for different physical and chemical applications like catalysis, photocatalysis, electronics and sensing.

Generally, the mechanism of photocatalysis in semiconductors involves the irradiation by light of energy equal or greater than the band gap energy of the catalyst to excite the electron from the valence band (VB) into the conducting band (CB), creating an excited electron-positive hole pair, known as the primary charge carrier species. The electron-hole pair can achieve redox reactions with electron donors and electron acceptors adsorbed on the semiconductor surface for the formation of highly oxidizing radical species (i.e., hydroxyl radicals), unless they recombine and return to the ground state and release the energy adsorbed as heat. These oxidizing species will react with the organic compounds to form the products of the reaction [1-3]. Figure 1.1 shows a representation of photocatalysis mechanism in TiO_2 reproduced from [4].

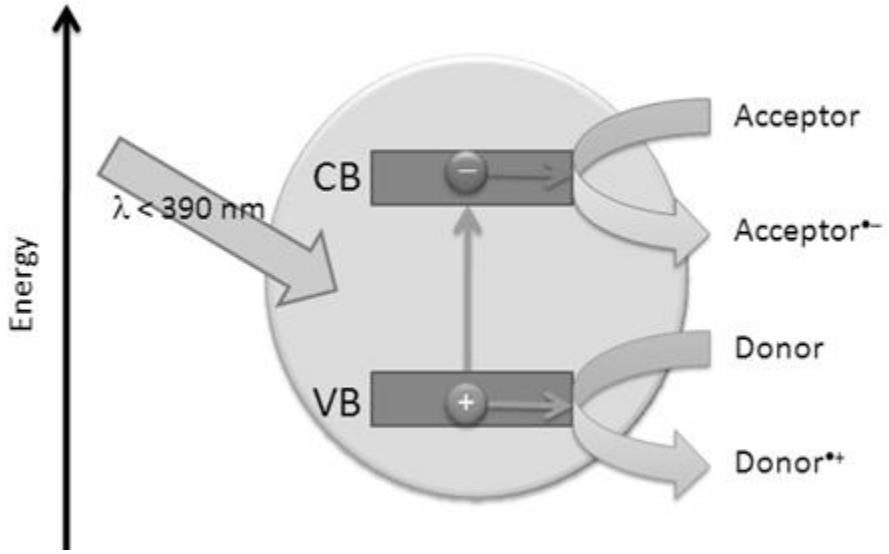

Figure 1.1 : Mechanism representation of photocatalysis [4]

1.2 Photocatalytic properties of nanostructured tungsten oxide

Tungsten oxide is a unique semiconductor. Because of its absorption of the visible light radiation and its suitable band gap, tungsten oxide is a favorable semiconductor for photocatalytic applications [5-7]. Bulk tungsten oxide has insufficient photocatalytic activity due to the comparatively little interaction between the radiation and the surface of tungsten oxide. However, the photocatalytic activity can be improved by nanostructured forms resulted from the drastic increasing in the specific surface area leading to an increase in the speed and yield of the photocatalytic reactions. Synthesis of nanostructured semiconductor can be achieved by many ways like sol-gel preparation and hydrothermal synthesis [8, 9] which considered common techniques for nanostructured materials synthesis [10]. In which methods, the crystallization is carried out in superheated aqueous solutions at relatively high pressure [11]. Different hydrothermally synthesized tungsten oxide were prepared [12] and it

has been reported that conditions like PH, presence of some salts and the solvent could hugely affect the nanosize and the morphology of the structure [13-15]. Field emission scanning electron microscope, X-ray diffractometer, particle size analyzer and BET surface area analyzer are used to characterize the morphology, crystal phase, particle size distribution and specific surface area respectively [16].

1.3 Platinum nanoparticles deposition on MOS

Because of its metallic character, platinum nanoparticles have an electron acceptor property which allows holding electrons and reduces their recombination with holes. This makes the holes more available. The presence of platinum nanoparticles on the surface of a metal oxide semiconductor (MOS) leads to huge enhancement of the photocatalytic properties for the oxidation reactions [17, 18]. The presence of platinum nanoparticles on MOS can be confirmed by transmission electron microscope [19, 20].

1.4 Graphene/MOS nanocomposites

Graphene, a two-dimensional with π-conjugation structure of carbon, has been used in several fields especially photocatalysis for enhancing the properties of the photocatalyst [21-23]. The mechanism of such enhancement could be by (i) Electron capturing and consequently reducing the recombination of electron-hole pairs, (ii) Increasing the specific surface area of the photocatalyst and (iii) Facilitating the absorption of the organic molecules by the strong π-π interaction with graphene [24]. The chemical exfoliation method of graphene synthesis can be achieved by; (i) oxidation of graphite into graphite oxide, (ii) exfoliation of graphite oxide layers into graphene oxide and (iii) finally, reduction of graphene oxide into graphene [25-27].

Metal oxide - graphene nanocomposite can be synthesized by many methods including the hydrothermal method where graphene oxide mixed with the metal oxide and a reducing agent [28]. Another method is by making metal oxide – graphene oxide nanocomposite and then reduce it photocatalytically into metal oxide - graphene nanocomposite [29]. Sonication of the suspension of metal oxide with graphene was also reported [30]. Metal oxide/graphene nanocomposite can be characterized by; field emission scanning electron microscope for the morphology and the composition, Raman spectrometer for graphene structure. Fourier transform infrared spectroscope for the bonding between metal oxide and graphene [31, 32].

In this study, different forms of nanostructured tungsten oxide were prepared and several techniques were employed for characterization including SEM, BET, PSA, XPS and UV-Vis spectroscopy. The photocatalytic activity toward oxidation of alcohols was investigated. Conditions, such as concentrations and ratios, for the oxidation of the selected alcohols were optimized. Platinum nanoparticles deposition and/or graphene addition on tungsten oxide were also achieved.

CHAPTER 2

LITERATURE REVIEW

2.1 Classical methods for oxidation of alcohols

Oxidation of alcohol to aldehyde and ketone is a very important reaction to a wide range of industries, such as pharmaceuticals and petrochemical industries [33]. There are many classical methods for oxidation of alcohols to aldehydes including Collins, Corey-Schmidt, Moffatt, Dess-Martin and NaOCl reaction. In Collins reaction, CrO_3 and pyridine are the reaction reagents; the reaction requires large excess of the reagents to be completed [34]. Corey-Schmidt reaction uses pyridinium dichromate as a reagent and under mild conditions to give aldehyde in conjugated alcohols and carboxylic acid in non-conjugated alcohols [35]. Moffatt reaction uses dimethyl sulfoxide and dicyclohexylcarbodiimide. Although it reacts under mild conditions but it suffers from elimination reactions especially in tertiary alcohols [36]. Dess-Martin reagent, periodinane is very selective reagent, which reacts with alcohols to give aldehydes while nitrogen and sulfur functions keep untouched [37]. NaOCl reacts selectively with 2° alcohols in presence of 1° alcohols to give the corresponding aldehydes [38]. Although alcohol can be oxidized to aldehyde by many ways, the need of high temperature and stoichiometric amount of the oxidant is the problems for those methods. Therefore, finding an alternative, inexpensive, environmental way is highly desirable [39].

2.2 Photocatalysis for oxidation of alcohols

2.2.1 Titanium dioxide

Titanium dioxide is a widely used photocatalyst because of its high catalytic activity due to the long lifetime of electron/hole pairs, the appropriate band edge position, and the good adsorption/desorption rate of reactants (especially oxygen) as well as good chemical stability [40]. Thus, TiO_2 is considered an effective photocatalyst for the degradation of organic compounds in gaseous and aqueous systems including the decomposition of acetaldehyde [41], acetone [42], chloroform [43], chlorophenols [44], and many other organic compounds. However, the formation of active oxygen species, such as $OH^{\bullet}$ and $O2^{\bullet-}$ that can randomly attack any position of the organic compound hinder the selectivity of TiO_2 as a photocatalyst under UV radiation [45]. The first attempt to use TiO_2 for the oxidation of benzyl alcohol to benzaldehyde was by Yurdakal et al.. The study uses nanostructured Rutile TiO_2 with different degree of crystallinity in aqueous solution. They reported on large effect of the crystallinity on the selectivity of the reaction [46]. Table 2.1 shows that Rutile TiO_2 with smaller crystallite size gives better selectivity and the best selectivity is 38 % for BA (benzyl alcohol) and 60% for MPA (4-methoxy benzyl alcohol) by using HP333 (home prepared catalyst). The improvement in case of MPA can be explained by considering the presence of the electron releasing methoxy group in the para position [46].

Table 2.1 : Effect of the crystallite size on the selectivity [46]

catalyst	SSA [m^2/g]	crystallite size [nm]	catalyst amount [g/L]	t_{irr} [h][b]	selectivity [% mol][b]
homogeneous				176	14.0
HP298	215		0.4	22	12.0
HP333	107	7	0.2	17	38.0
HP333	107	7	0.4	8.4	38.2
HP333	107	7	0.6	8.95	37.7
HP333-MBA	107	7	0.4	2.36	60.0
HP673	35	13	0.4	6	12.0
HP973	4	41	0.4	9.4	9.9
SA	2.5	52	0.4	3.75	9.2
SA-MBA	2.5	52	0.4	2.15	20.9

[a] The experimental results refer to BA oxidation, except that indicated as HP333-MBA and SA-MBA, referring to MBA. [b] Irradiation time (*t*irr) and selectivity (to aldehyde) are calculated for alcohol conversion of 50%.

Li et al. reported that single-crystalline rutile TiO_2 nanorods can partially oxidize benzyl alcohol into benzaldehyde with high selectivity under visible light radiation, 27% conversion and > 99 % selectivity were reported in this work while previous works show that rutile nanoparticles TiO_2 has selectivity of 38 % and 42 % as shown in figure 2.1. By such materials, working under visible light radiation increases the selectivity and decrease the conversion of the reaction [47]. To improve the conversion of the reaction of TiO_2 under visible light radiation, Higashimoto et al. suggested working under gas phase purged by pure oxygen. The study reported that the photocatalytic oxidation of benzyl alcohol into benzaldehyde performed at high conversion rate of > 99 % and high selectivity of > 99 % on TiO_2 in the presence of O_2 under visible light irradiation [48]. In another study, Higashimoto et al. suggested that modifying the surface of TiO_2 with iron (III) ion improves the conversion under visible light radiation. Table 2.2 [48] demonstrates that only iron (III) ion improved the conversion of the reaction from 47% to 74% (the initial concentration is 50 µmol) while other ions decrease the conversion compared to pure TiO_2 of the reaction. The key factors for generating such highly active photocatalytic system are considered as follows: (1) the efficient electronic transitions from the energy levels constructed by the oxygen 2p orbitals of the alcoholate species hybridized with the occupied Fe 3d orbitals to the CB of the TiO_2, (2) electron transfers to the unoccupied Fe 3d orbitals as the acceptor levels accompanied by O_2 reduction with two and/or four electrons [49].

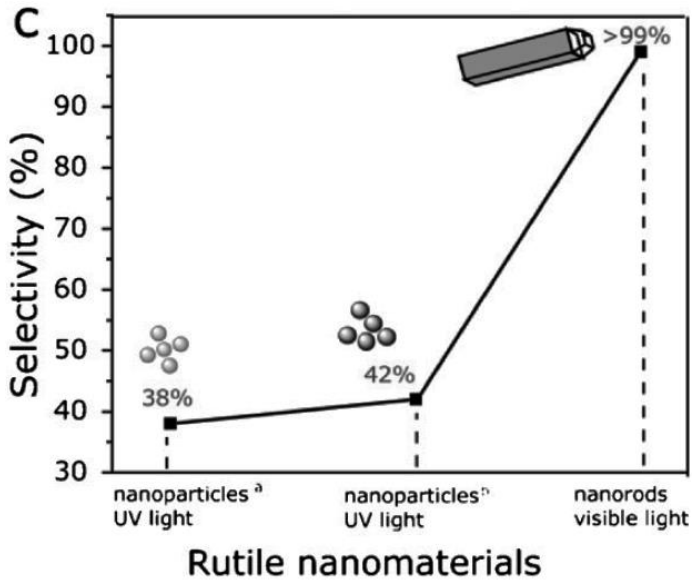

Comparison of selectivity for partial oxidation of benzyl alcohol over obtained rutile TiO_2 nanorods under visible-light irradiation with the reported results for rutile nanoparticles under UV light irradiation.

Figure 2.1 : Effect of working on visible light radiation on selectivity [47]

Table 2.2 : Effect of loaded metal ion on TiO_2 on the reaction yields [49]

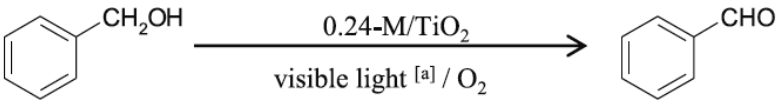

Run	Time (h)	M[b]	Yields (μmol)
1	1	–	23.7
2	1	Fe^{3+}	37.3
3	1	Ag^{+}	22.8
4	1	Rh^{3+}	21.1
5	1	V^{5+}	17.5
6	1	Ru^{3+}	16.5
7	2	Ce^{3+}	18.3
8	2	Mn^{2+}	17.6
9	2	Au^{3+}	12.6
10	2	Pt^{4+}	8.5
11	4	Cu^{2+}	0.6
12	4	Pd^{2+}	0.3

[a]Visible-light irradiation with 18,000 lux from blue LED lamp. [b]Loading amounts of metal ions (M): 0.24 atomic%.

2.2.2 Semiconductors modified by transition metals

Transition metals deposition on the surface of the semiconductor is performed in order to improve its photocatalytic properties. Pan et al. examined the effect of platinum, palladium and silver nanoparticles deposition on the photocatalytic activity of TiO_2 toward oxidation of benzyl alcohol under visible light radiation. The aforementioned transition metals were reported to enhance the photocatalytic activity with selectivity >99%, while Pd/TiO_2 shows the highest conversion with 65 % then platinum with 23 %, silver shows only 12 % conversion, figure 2.2, reproduced from [50]. Another study made by Zhang et al. showed the photocatalytic properties of palladium on cerium oxide on the oxidation of alcohol under visible light radiation. The study compared between Multi-Pd Core@CeO_2 Shell nanocomposite and supported Pd/CeO_2 nanocomposite, Table 2.3 (reproduced from [51]). It reported Pd Core@CeO_2 Shell nanocomposite with higher conversion and selectivity than the supported one. The table shows decreasing in the conversion in methyl, methoxy and nitro group on the benzene ring, while it shows improvement in case of halogen substituent Cl and F [51].

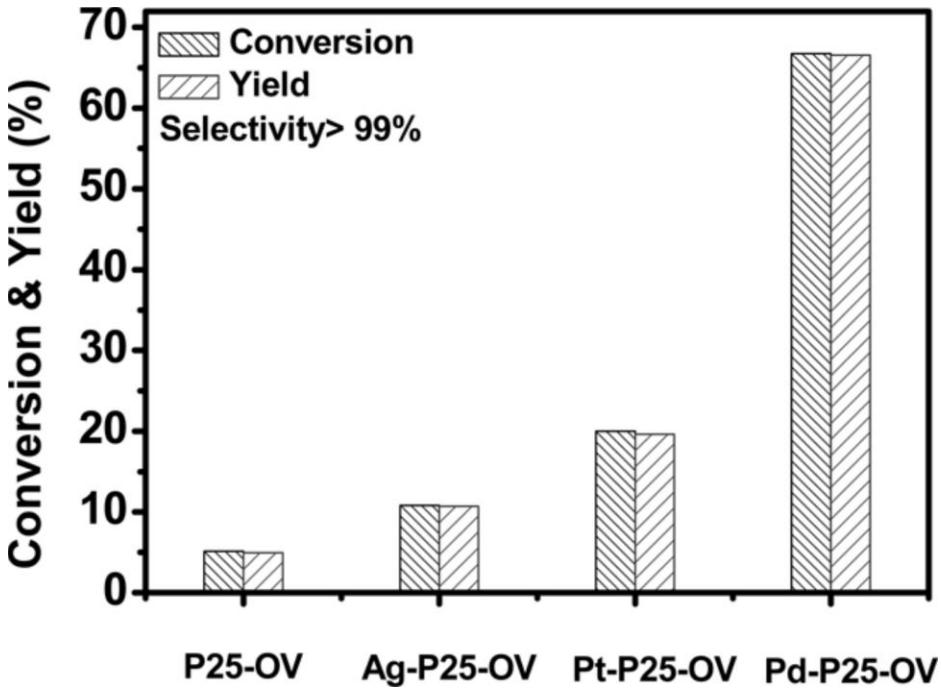

Figure 2.2 : Effect of different noble metal on the conversion [50]

Table 2.3 : Effect of different alcohol on selectivity and conversion of Pd/CeO_2 [51]

Entry	Substrate	Product	Time (h)	$Pd@CeO_2$			Pd/CeO_2		
				Conv. (%)	Yield (%)	Selec. (%)	Conv. (%)	Yield (%)	Selec (%)
1	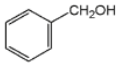	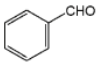	20	28	28	100	7	5	71
2	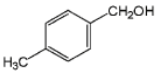	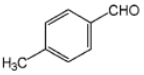	20	10	10	100	5	4	74
3	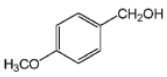	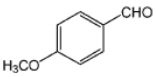	20	12	12	100	8	6	73
4	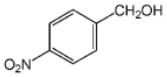	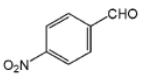	20	8	8	100	4	3	80
5	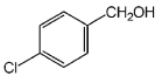	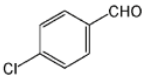	20	35	34	96	15	9	58
6	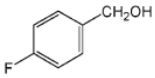	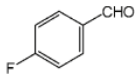	20	42	31	74	13	8	65

Tanaka et al. reported on the gold nanoparticles loaded on ceria for photocatalytic applications. Au/CeO_2 was prepared by the multistep (MS) photodeposition method and by using the single-step (SS) photodeposition method. The MS- and SS Au/ CeO_2 were used for selective oxidation of benzyl alcohols to corresponding benzaldehyde in aqueous suspensions under irradiation by visible light from a green LED. It was reported that the selectivity is (>99%) at >99% conversion of benzyl alcohol. In the study also a comparison between photocatalytic activity of MS- and SS Au/ CeO_2 for different sort of alcohols, indicated that both methods give perfect selectivity in all alcohols. It also shows that MS Au/ CeO_2 give better conversion than SS Au/ CeO_2, Table 2.4. The study showed that gold nanoparticles in MS are bigger than those in SS. This indicates that the external surface area of Au nanoparticles rather than the Au content is one of the important factors controlling the reaction rate of Au/CeO_2 under visible light irradiation [52].

Table 2.4 : Effect of different alcohol on selectivity and conversion on Au/CeO_2 [52]

Method	Substrate	Product	Time / h	Conv.[b] / %	Selectivity[b] / %
SS	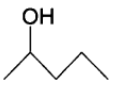	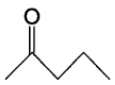	25	39	>99
MS				45	>99
SS	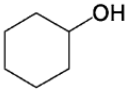	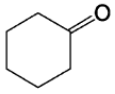	24	45	>99
MS				59	>99
SS	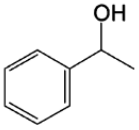	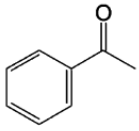	36	33	>99
MS				45	>99
SS	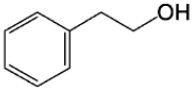	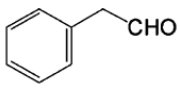	56	13	>99
MS				17	>99

[a] Photocatalytic reactions: Au/CeO2, 50 mg; water, 5 cm3; O2, 1 atm; green LED, 1.7 mW cm−2.
[b] Determined by GC using the internal standard method.

2.2.3 Semiconductors modified by graphene

There are different types of graphene that have different properties, and consequently suitable for specific applications. For instance, graphene with large sheet size isn't semiconductor because of its zero band gap. However, when graphene has narrow widths (<~30 nm), the energy gap fluctuate between 0 to 0.5 eV [53]. Bilayers and multilayers graphene have smaller specific surface area than monolayer graphene. Thus, they improve the photocatalytic properties when introduced to semiconductors less efficiently compared to monolayer graphene [54]. Graphene with oxygen containing functionalities or graphene oxide is not stable under irradiation of the semiconductor because it can be reduced into graphene [55]. However, graphene is stable material and can be better photocatalyst supporter than graphene oxide. Zhang et al. investigated the effect of graphene on the photocatalytic properties of cadmium sulfide on the photocatalytic oxidation of benzyl alcohol to corresponding aldehyde, figure 2.3(reproduced from [56]). Comparing pure CdS with mixtures of different ratios of CdS/graphene, the conversion was enhanced with optimum ratio of 5% graphene with 43 % conversion and > 99% selectivity. However the conversion was reported to decrease under higher graphene content. Relatively high weight ratio of Gn in CdS/graphene nanocomposites would lower the contact surface of semiconductor CdS nanoparticles with the light illumination, thus leading to a decreased photocatalytic activity, which accounts for the decline in the conversion [56].

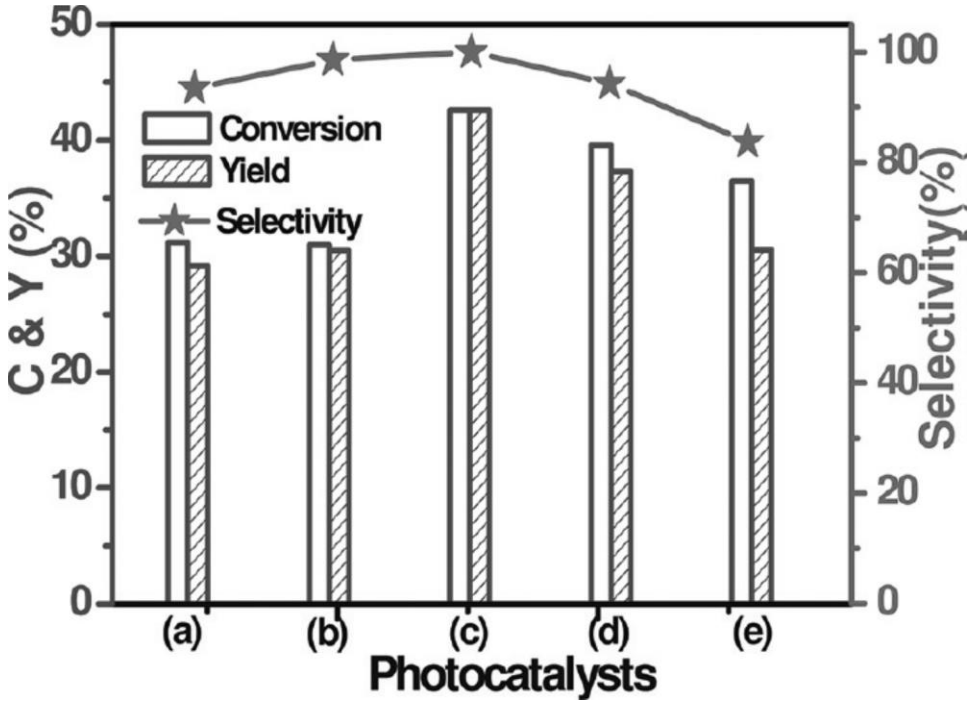

Photocatalytic selective oxidation of benzyl alcohol to benzaldehyde under the visible light irradiation for 4 h over the as-prepared samples: (a) blank-CdS; (b) CdS_1% GR; (c) CdS_5% GR; (d) CdS_10% GR; (e) CdS_30% GR nanocomposites. Note: C & Y is short for conversion and yield.

Figure 2.3 : Effect of graphene content in CdS/Gn photocatalytic activity [56]

In another study, Yang et al. prepared fullerene, carbon nanotube, and graphene/TiO_2 nanocomposite, and compared their photocatalytic properties for the oxidation of benzyl alcohol under visible light irradiation. The study investigated different carbon ratios and reported on the photocatalytic activities of the composites with optimum ratios are TiO_2−0.1% Gn, TiO_2−0.5% CNT, and TiO_2−1.0% C60. The conversions of benzyl alcohol are all close to each other (ca. 40%), along with the selectivity higher than 95%. The present work suggested that the photocatalytic performance of TiO_2−carbon is significantly affected by the preparation methods. The change in preparation methods causes the difference in structural composition and synergetic interaction between TiO_2 and carbon, which thus influences the photocatalytic performance of TiO_2−carbon composites. Graphene is more popular than other nanocarbon materials (CNT and C60) at present with regard to synthesis and application of

semiconductor−carbon composite photocatalysts. So it seems too early to draw a definitely decisive answer for graphene's unique superiority to other carbon allotropes on improving the photocatalytic performance of semiconductors [57].

Using tungsten oxide for photocatalytic applications, such as O_2 production, H_2 Production, and organic compound degradation, were reported in literatures as below:

Application	**Irradiation**	**Ref. Number**
H_2 production	Visible	[5]
O_2 production	Simulated sunlight	[6]
Methylene blue degradation	UV	[7]

However, photocatalytic oxidation of alcohols using tungsten oxide isn't to the best of our knowledge reported in literature.

CHAPTER 3

RESEARCH OBJECTIVE

The aim of this study was:

1) To synthesize nanostructured tungsten oxide hydrothermally and examine the effect of the presence of hydrochloric acid and oxalic acid on the morphology and nanosize of the prepared crystals, and investigate its photocatalytic activity toward oxidation of some alcohols in aqueous solutions under simulated sunlight.
2) To improve the photocatalytic activity of the prepared nanostructured tungsten oxide by:
   A) The deposition of platinum nanoparticles on nanostructured tungsten oxide.
   B) Synthesis of nanocomposite tungsten oxide/graphene.
   C) Synthesis of the nanocomposite platinum/tungsten oxide/graphene.
3) To characterize the synthesized materials by field emission scanning electron microscope, X-ray diffractometer, Surface Area & Porosity Analyzer and Nano/Micro Particles size Analyzer, UV-Vis spectroscope, X-ray photoelectron spectroscope, transmission electron microscope, Raman spectrometer and Fourier transform infrared spectroscope.
4) To optimize the process in order to achieve the highest conversion and selectivity of the selected alcohols to their corresponding aldehydes including optimizing time, alcohol concentration, catalyst concentration, percentage of the platinum and graphene in the compositions and the presence of oxygen and nitrogen in the solution.

CHAPTER 4

METHODOLOGY & RESEARCH DESCRIPTION

4.1 Chemicals

The following chemicals were used; Sodium tungstate dehydrate, potassium dichromate (Sigma Aldrich >99%), hydrochloric acid (Sigma Aldrich >37%), oxalic acid (Fisher scientific >99.99%), sulfuric acid (Eurostar scientific 98%), ethanol (sigma Aldrich >99.5%), graphite (Fluka Chemical 99%), tungstic acid, hydrazine hydrate (Janssen Chimica 80%), hexachloroplatinic acid, benzyl alcohol, benzaldehyde, 4-methoxy benzyl alcohol (Sigma Aldrich >99.99%), Cinnamyl alcohol (Acros Organics 98% trans) , chloroform (Sigma Aldrich >99.8%), O_2 and N_2 cylinders (99.9999%).

4.2 Synthesis

4.2.1 Nanostructured tungsten oxide synthesis

Three different nanostructured tungsten oxides were synthesized by hydrothermal process. The first one (WO_3-A) was prepared by mixing 1.42 gram of sodium tungstate with excessive amount of hydrochloric acid (3 ml of 37 %) in 65 ml deionized water. After stirring, the resulting suspension was transferred into a 100 ml Teflon-lined hydrothermal vessel and was heated at 200 for 24 hours. Afterward, the catalyst was centrifuged, washed with water and dried at 80°C. The second one (WO_3-B) was prepared by replacing hydrochloric acid with oxalic acid (equivalent weight of sodium tungstate) in the aforementioned method, and the last one (WO_3-C) was prepared by replacing the excessive amount of hydrochloric acid with

equivalent amount of hydrochloric acid and 0.142 gram of oxalic acid, the following equations explain the synthesis steps:

$$Na_2WO_4 + 2\ HCl \rightarrow 2\ NaCl + H_2WO_4$$

$$H_2WO_4 + heat \rightarrow H_2O + WO_3$$

The bulk tungestin oxide prepared by heating tungestic acide for 12 hours at 200 ^{0} C.

4.2.2 Platinum nanoparticles deposition on tungsten oxide

The deposition of Pt onto WO_3 surface was performed photocatalytically; To 100 mL water, required amount of hexachloroplatinic acid (H_2PtCl_6) and (WO_3) was added. The suspension was stirred and purged with high purity nitrogen gas for about 30 min, to remove dissolved oxygen 10 vol. % methanol was added as an electron donor. Irradiations were carried out under simulated sunlight for 4 hours. After irradiation, the metal loaded catalyst was washed with ethanol and separated through centrifugation and dried [58]. Below is the proposed equation for the reduction reaction that takes place during the deposition of the platinum:

$$H_2PtCl_6 + 4\ e^- + h\upsilon \rightarrow Pt + 2H^+ + 6\ Cl^-$$

4.2.3 Graphene nanocomposite synthesis

4.2.3.1 Synthesis of graphene nanosheets:

5g of graphite was added into 200 ml concentrated sulfuric acid (98%), and the resulting solution was transferred to an ice bath and 35g of potassium dichromate was added very slowly and the solution was kept under stirring for 7 days at room temperature. The resulting graphite oxide was washed thoroughly and then exfoliated to graphene oxide by

ultrasonicator. Graphene oxide was reduced into graphene by stirring graphene oxide solution with hydrazine for 24 h at 95°C and the final product were washed, and vacuum-dried [59].

4.2.3.2 Synthesis of nanocomposites:

Synthesis of WO_3/Gn nanocomposite was carried out by two methods. In the first method, WO_3 was mixed with graphene layers in an ethanol solution. The solution was homogenized by ultrasonicator, followed by centrifuging, washing and drying. In the second method, WO_3 was mixed with graphene layers and homogenized by ultrasonicator in in 65 ml water, After that, the solution was transferred into a 100 ml Teflon-lined hydrothermal vessel and heated at 200°C for 24 hours where the deposition of photocatalyst on graphene surface was achieved. The products were separated by centrifugation, washed and dried. The synthesis of Pt/WO_3/Gn nanocomposite was carried out by photocatalytic deposition of platinum on hydrothermally prepared WO_3/Gn nanocomposite. Table 4.1 shows the list of the prepared catalysts in this study [60].

Table 4.1 : List of the prepared catalysts

1	Nanostructured WO_3-A (prepared in the presence of hydrochloric acid)
2	Nanostructured WO_3-B (prepared in the presence of oxalic acid)
3	Nanostructured WO_3-C (prepared in the presence of oxalic acid and hydrochloric acid)
4	0.5 % platinum in Pt/WO_3
5	1 % platinum in Pt/WO_3
6	1.5 % platinum in Pt/WO_3
7	2 % platinum in Pt/WO_3
8	2.5 % platinum in Pt/WO_3
9	0.5 % Graphene in WO_3/Gn mix.
10	1 % Graphene in WO_3/Gn mix.
11	2.5 % Graphene in WO_3/Gn mix.
12	5 % Graphene in WO_3/Gn mix.
13	WO_3/Gn nanocomposite
14	Pt/WO_3/Gn nanocomposite

4.3 Characterization

Tungsten oxide was characterized by Field emission scanning electron microscope, X-ray diffractometer, Surface Area & Porosity Analyzer and Nano/Micro Particles Analyzer, UV-Vis spectroscope, X-ray photoelectron spectroscope. The presence of platinum on tungsten oxide surface was characterized by transmission electron microscope. Graphene nanocomposites were characterized by Field emission scanning electron microscope, Raman spectrometer and Fourier transform infrared spectroscope.

4.4 Photocatalytic evaluation

The photocatalytic activity of nanostructured tungsten oxide and its nanocomposites on the oxidation of the aforementioned alcohols were evaluated in a photochemical reactor and the Irradiation was performed using simulated sunlight lamp. Experimental parameters, such as different time, conditions, concentrations and catalyst compositions, were optimized. Benzyl alcohol was selected to be model alcohol in the study. Table 4.2 shows the list of photocatalytic experiments.

Table 4.2 : List of photocatalytic reactions

1	Bulk WO_3
2	Nanostructured WO_3-A
3	Nanostructured WO_3-B
4	Nanostructured WO_3-C
5	Nanostructured WO_3-C without the irradiation
6	Irradiation without catalyst
7	Concentration of the catalyst : 0.5 g/L
8	Concentration of the catalyst : 1 g/L
9	Concentration of the catalyst : 2 g/L
10	Concentration of the catalyst : 3 g/L
11	Concentration of the reactant : 0.5 mmol/L
12	Concentration of the reactant : 1 mmol/L
13	Concentration of the reactant : 1.5 mmol/L
14	Concentration of the reactant : 2 mmol/L
15	Platinum percentage in Pt/WO_3 : 0.5 %
16	Platinum percentage in Pt/WO_3 : 1 %
17	Platinum percentage in Pt/WO_3 : 1.5 %
18	Platinum percentage in Pt/WO_3 : 2 %
19	Platinum percentage in Pt/WO_3 : 2.5 %
20	4-methoxy benzyl alcohol with Pt/WO_3
21	Cinnamyl alcohol with Pt/WO_3
22	O_2 bubbling under optima
23	N_2 bubbling under optima
24	Graphene percentage in WO_3/Gn : 0.5 %
25	Graphene percentage in WO_3/Gn : 1 %
26	Graphene percentage in WO_3/Gn : 2.5 %
27	Graphene percentage in WO_3/Gn : 5 %
28	Benzyl alcohol with WO_3/Gn nanocomposite
29	4-methoxy benzyl alcohol with WO_3/Gn nanocomposite
30	Cinnamyl alcohol with WO_3/Gn nanocomposite
31	Benzyl alcohol with Pt/WO_3/Gn nanocomposite
32	4-methoxy benzyl alcohol with Pt/WO_3/Gn nanocomposite
33	Cinnamyl alcohol with Pt/WO_3/Gn nanocomposite

4.5 Samples analysis:

4.5.1 Samples preparation

The alcohols in the matrix were analyzed qualitatively and quantitatively every 2 hours in 12 hours. The samples were collected from the reactor via syringe and filtered to get rid of the insoluble catalyst by the syringe filter. Then they were extracted by adding 2 ml of chloroform to an equivalent volume of the reaction solution, shaking them vigorously for two minutes. The collected chloroform layer was analyzed by GC-MS via autosampler.

4.5.2 Calibration curves for quantification of the studied alcohols

To calculate the concentration of the alcohols in the matrix, external standard calibration was applied by preparing series of known concentrations of the alcohols (5, 1.5, 1, 0.5, 0.25 and 0.125 mmol/L) in water, then extracted and injected in GC-MS. The conversion of the reaction calculated by the following equations:

$$\text{Conversion (\%)} = [(C_0 - C_{alcohol}) / C_0] \times 100$$

Where, C_0 is the initial concentration of alcohol, and $C_{alcohol}$ the concentration of benzyl alcohol at determined time during the reaction.

Because of its highly volatile properties, aldehydes were unable to detect quantitatively, but because of the absence of any byproduct in the chromatograph, aldehydes were considered to be the only product with >99% selectivity.

Figure 4.1 shows the calibration curves for quantification of the studied alcohols and it shows R-squared value close to one in all alcohols indicating to very good linearity and precise measurements. Appendix A shows details GC-MS running parameters for the studied alcohol.

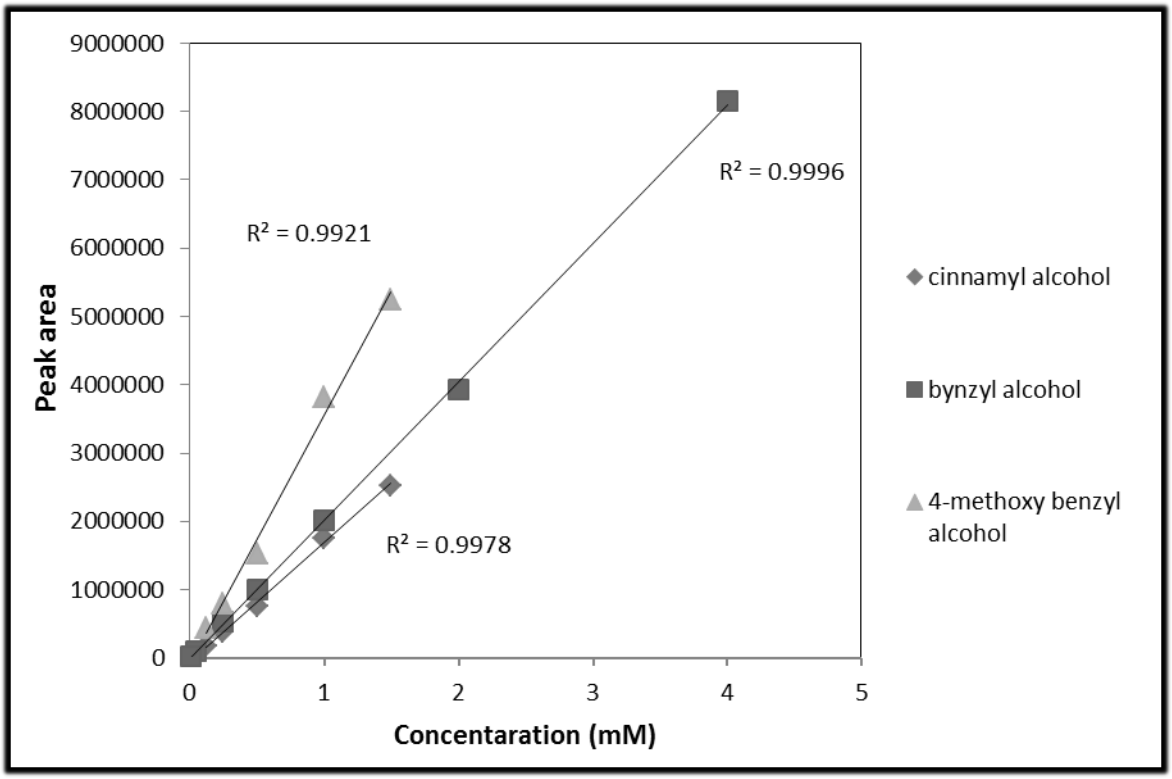

Figure 4.1: Calibration curves for quantification of the studied alcohols

CHAPTER 5

RESULTS AND DISCUSSION

5.1 Catalysts characterization

5.1.1 Characterization of nanostructured tungsten oxide

The three synthesized forms of nanostructured tungsten oxide, WO_3-A, WO_3-B and WO_3-C were characterized by X Ray Diffractometer, surface area and porosity analyzer (BET), particles size analyzer, field emission scanning electron microscope, UV-Vis spectroscope and X-ray photoelectron spectroscope.

5.1.1.1 X Ray Diffraction analysis

X-Ray diffraction was performed for WO_3-A, WO_3-B, WO_3-C. Figure 5.1 and figure 5.3 shows XRD pattern of WO_3-A and WO_3-C respectively, which confirmed that WO_3-A and WO_3-C have monoclinic crystalline structure. However, XRD pattern of WO_3-B (figure 5.2) confirmed that it has hexagonal crystalline structure. It is worth to mention that previous study suggests that monoclinic tungsten oxide has better photocatalytic activity than hexagonal tungsten oxide [61].

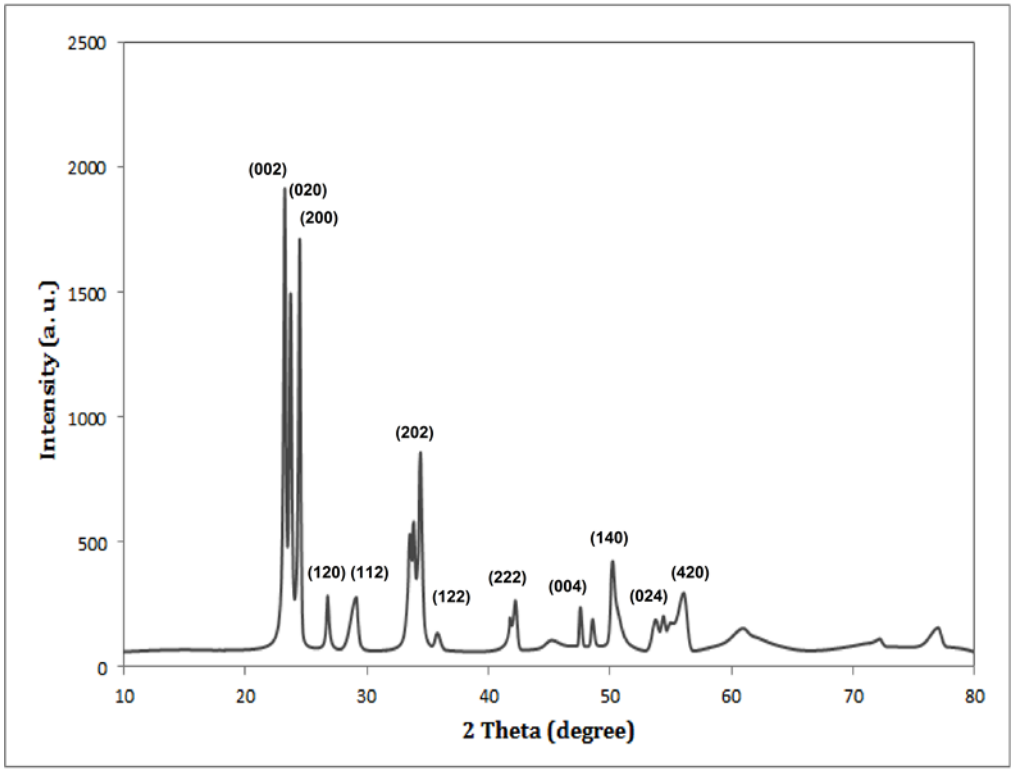

Figure 5.1 : XRD pattern of WO_3-A

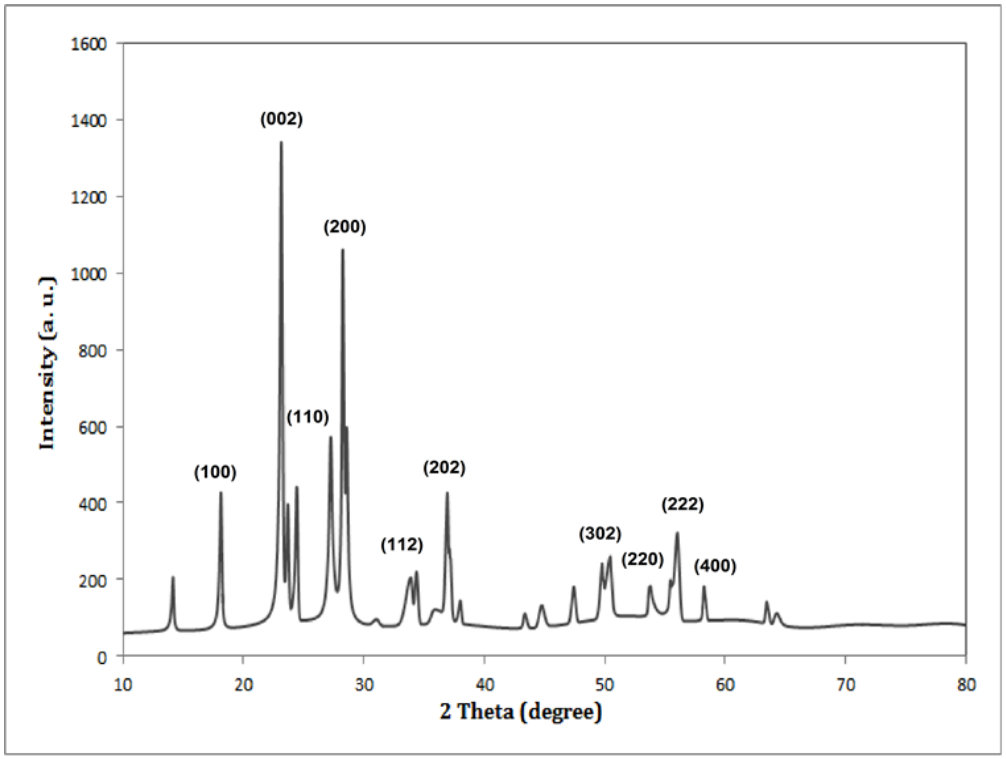

Figure 5.2 : XRD pattern of WO_3-B

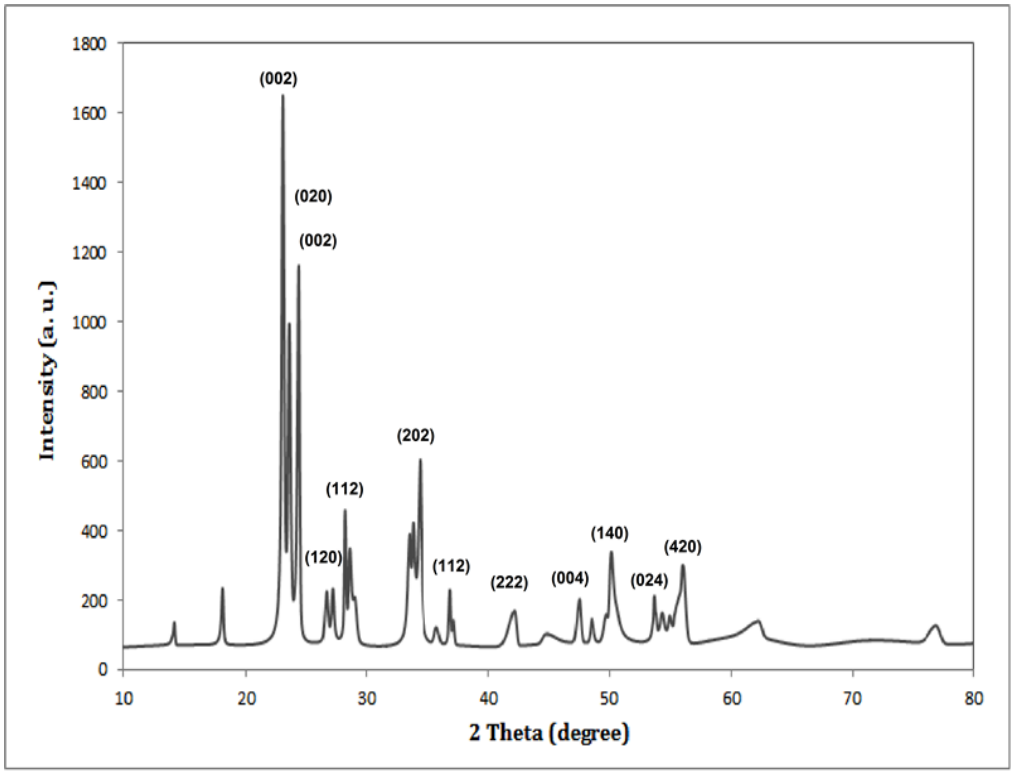

Figure 5.3 : XRD pattern of WO_3-C

5.1.1.2 Surface area and porosity analysis

The prepared nanostructured tungsten oxides were characterized by surface area and porosity analyzer to examine their porosity and surface area, Figure 5.4, figure 5.5 and figure 5.6 are the Isothermal linear plots of WO_3-A, WO_3- B, WO_3-C respectively. Where WO_3-A has the lowest Langmuir surface area with (7.0155 m^2/g), WO_3-B has the highest Langmuir surface area with (58.3968 m^2/g). This is probably due to the presence of oxalic acid in the autoclave, which decomposes into CO_2 gas which increases the porosity and consequently the surface area. WO_3-C (prepared in the presence of 10% oxalic acid) shows less porosity than WO_3-A and more porosity than WO_3-B with Langmuir surface area (40.4485 m^2/g). The BJH Adsorption average pore width of WO_3-A, WO_3- B and WO_3-C are 427.012 Å, 131.368 Å and 84.511 Å respectively, Appendix B shows the detailed BET analysis of WO_3.

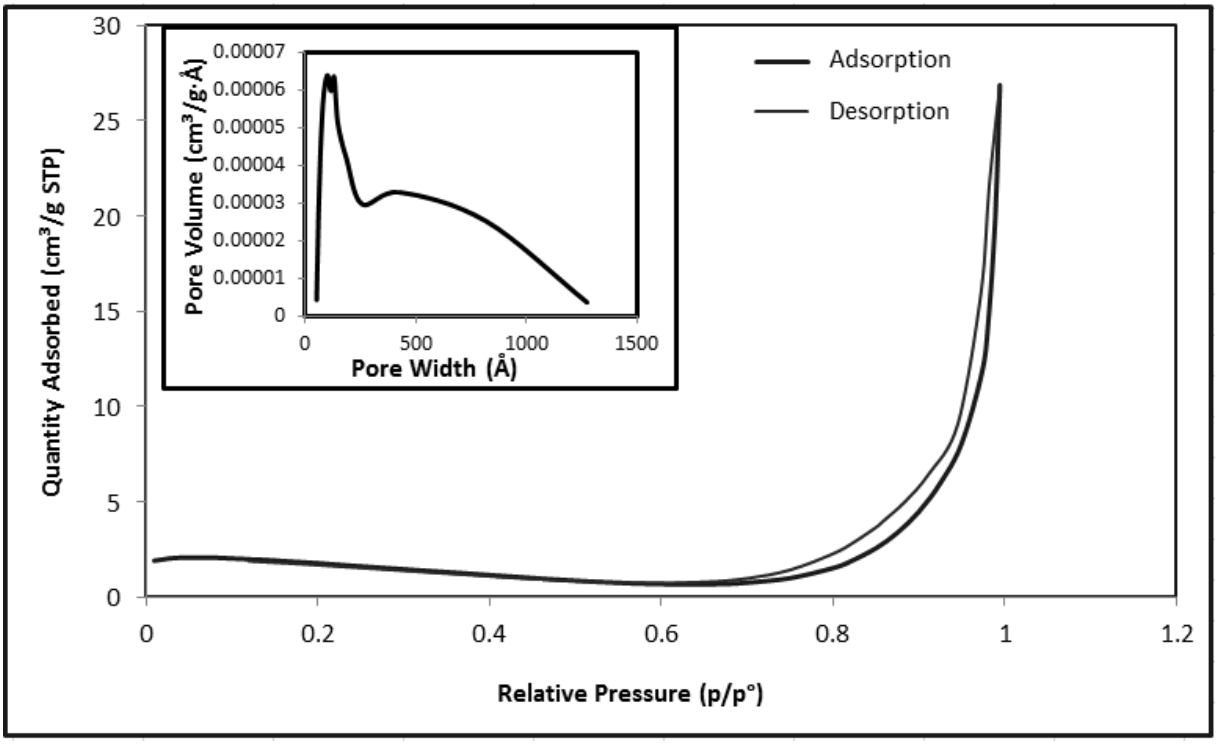

Figure 5.4 : Isothermal linear plot and pore width distribution of WO_3 - A

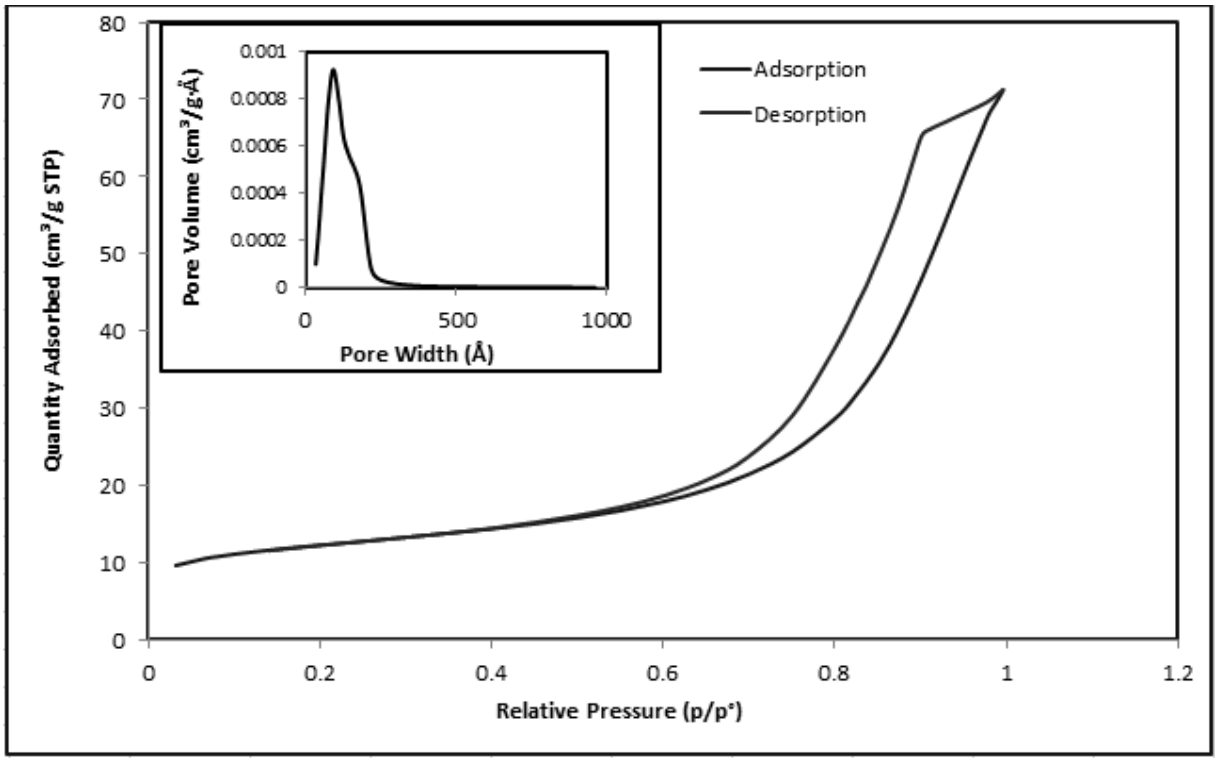

Figure 5.5 : Isothermal linear plot and pore width distribution of WO_3 - B

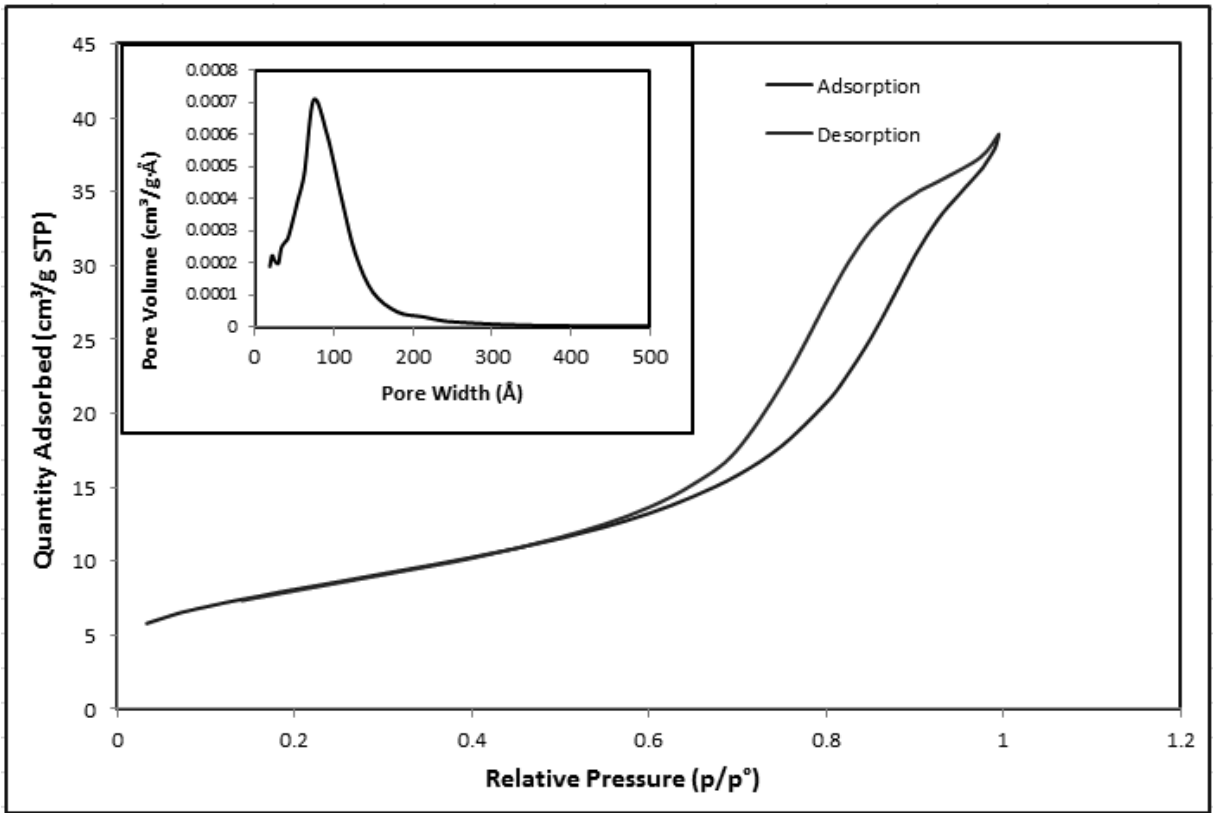

Figure 5.6 : Isothermal linear plot and pore width distribution of WO_3-C

5.1.1.3 Particles size analysis

The surface area of a material comes from the outer surface and the pores. BET provides the surface area of the overall surface. Particle size analyzer provides the surface area of the particles as a spherical entity regardless of the surface that came from pores. Figure 5.7 shows the particle distribution of WO_3-A with 71 % of the particles larger than 30 microns and 80% larger than 10 microns. Figure 5.8 shows the particle distribution of WO_3-B with 70 % of the particles smaller than 5.5 microns and 80% smaller than 50 microns. The analysis also shows that the mean size (Mz) of WO_3-A is 109.0 and the calculated surface is 1.128, whereas Mz of WO_3-B is 38.8 and the calculated surface is 5.13. Appendix C shows the detailed Particles size analysis of WO_3-A and WO_3-B.

5.1.1.4 Field emission scanning electron microscopy analysis

To examine the morphology and the nano size of the prepared WO_3, filed emission scanning electronic microscope were employed. Figure 5.9 depicts SEM photograph of WO_3-A indicating that the crystals size is around 30 nanometers and close to spherical morphology. Figure 5.10 shows SEM photograph of WO_3-B with crystals size of around 50 nanometers with organized squired shape crystals. Such crystals shape of tungsten oxide were reported by hydrothermal treatment using L(+)-tartaric acid or citric acid as assistant agents [62]. Figure 5.11 shows that WO3-C has the crystals size of around 20 nanometers with spherical shape.

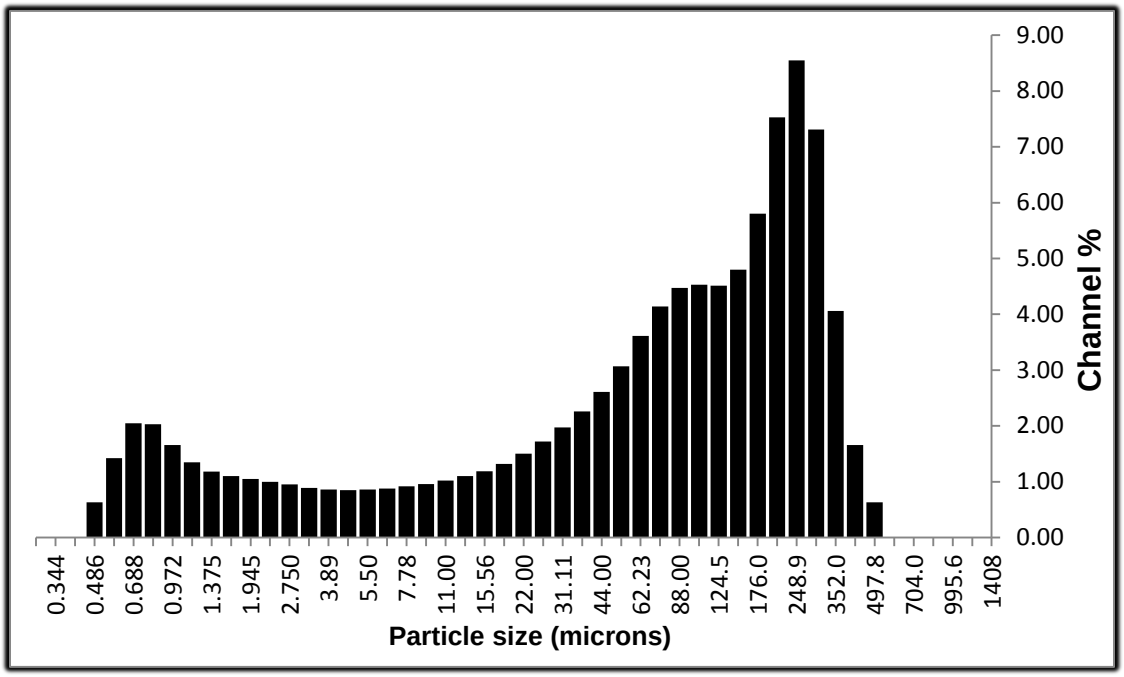

Figure 5.7 : Particle size distribution of WO_3-A

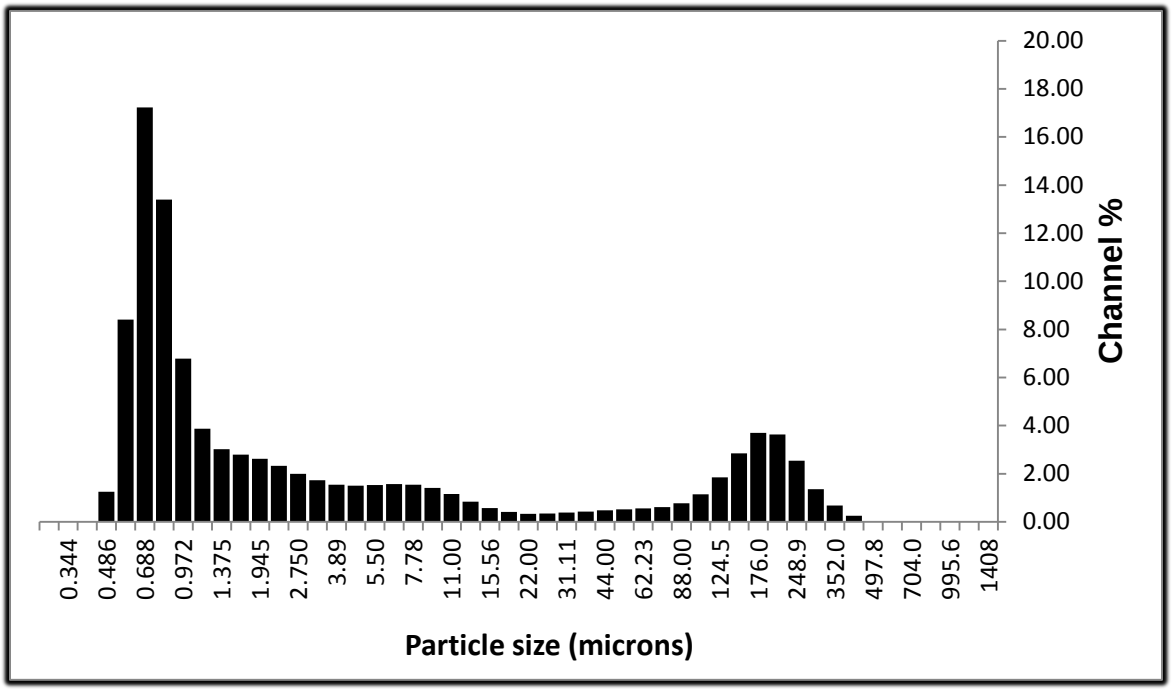

Figure 5.8 : Particle size distribution of WO_3-B

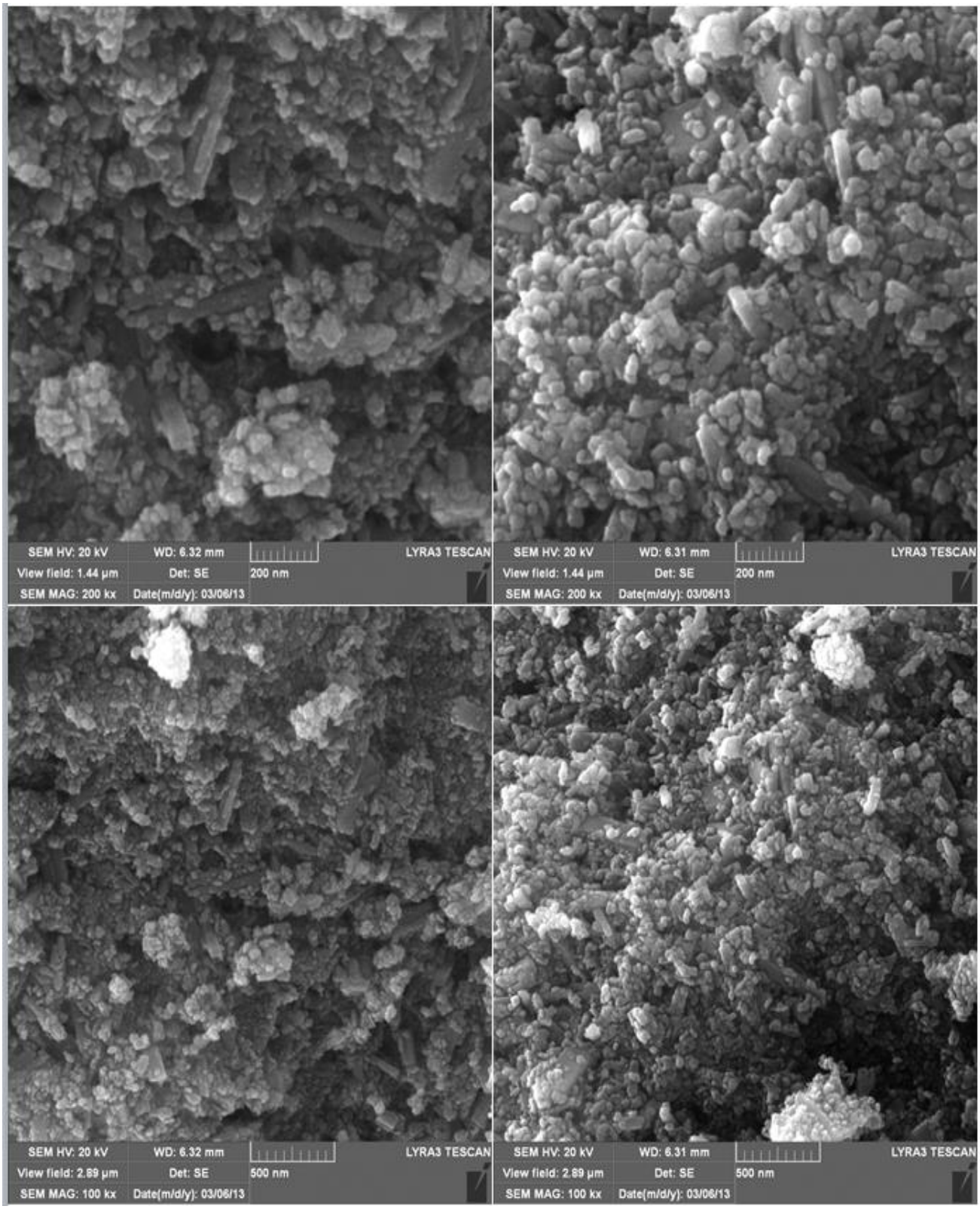

Figure 5.9 : SEM images of WO_3-A

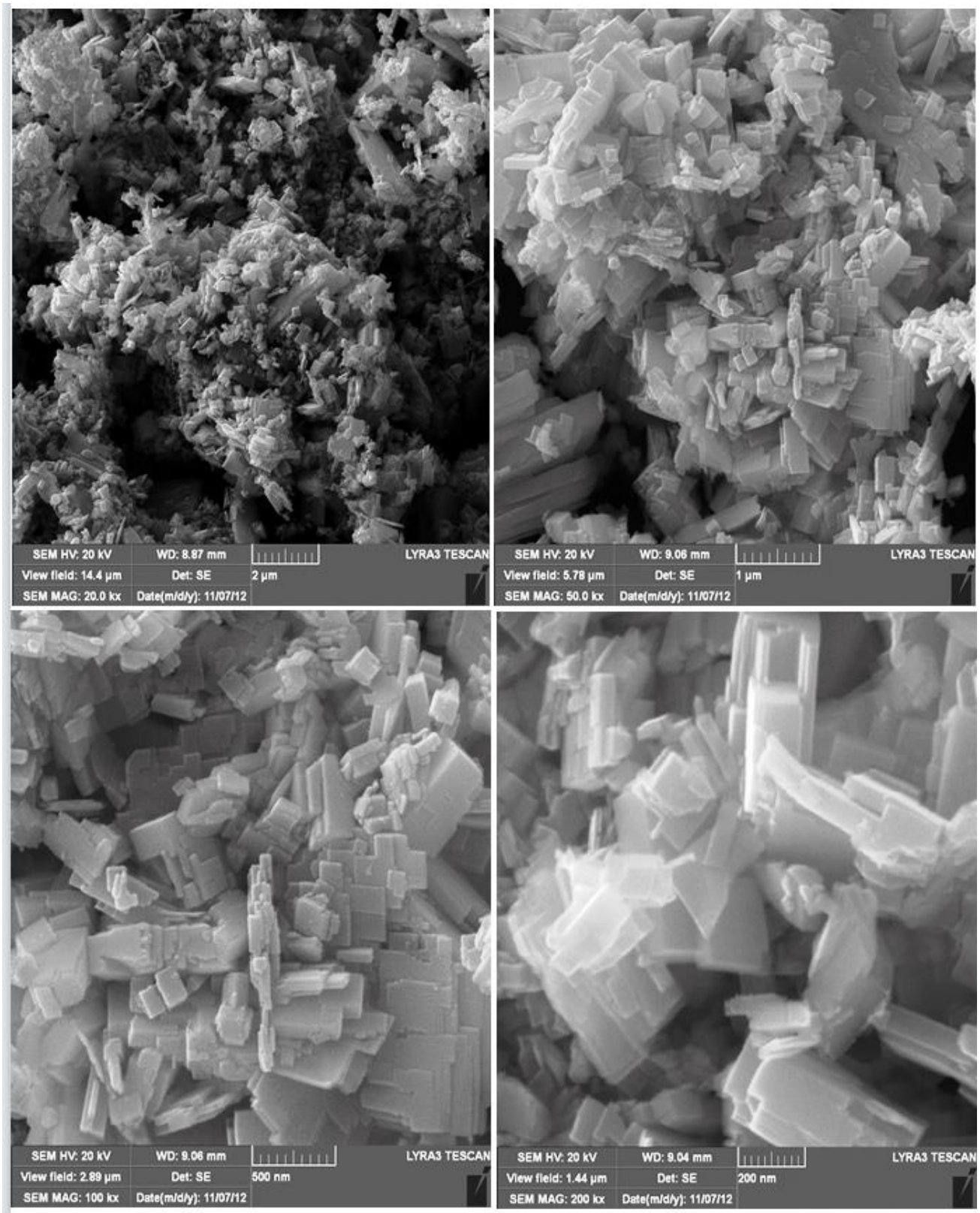

Figure 5.10 : SEM images of WO_3-B

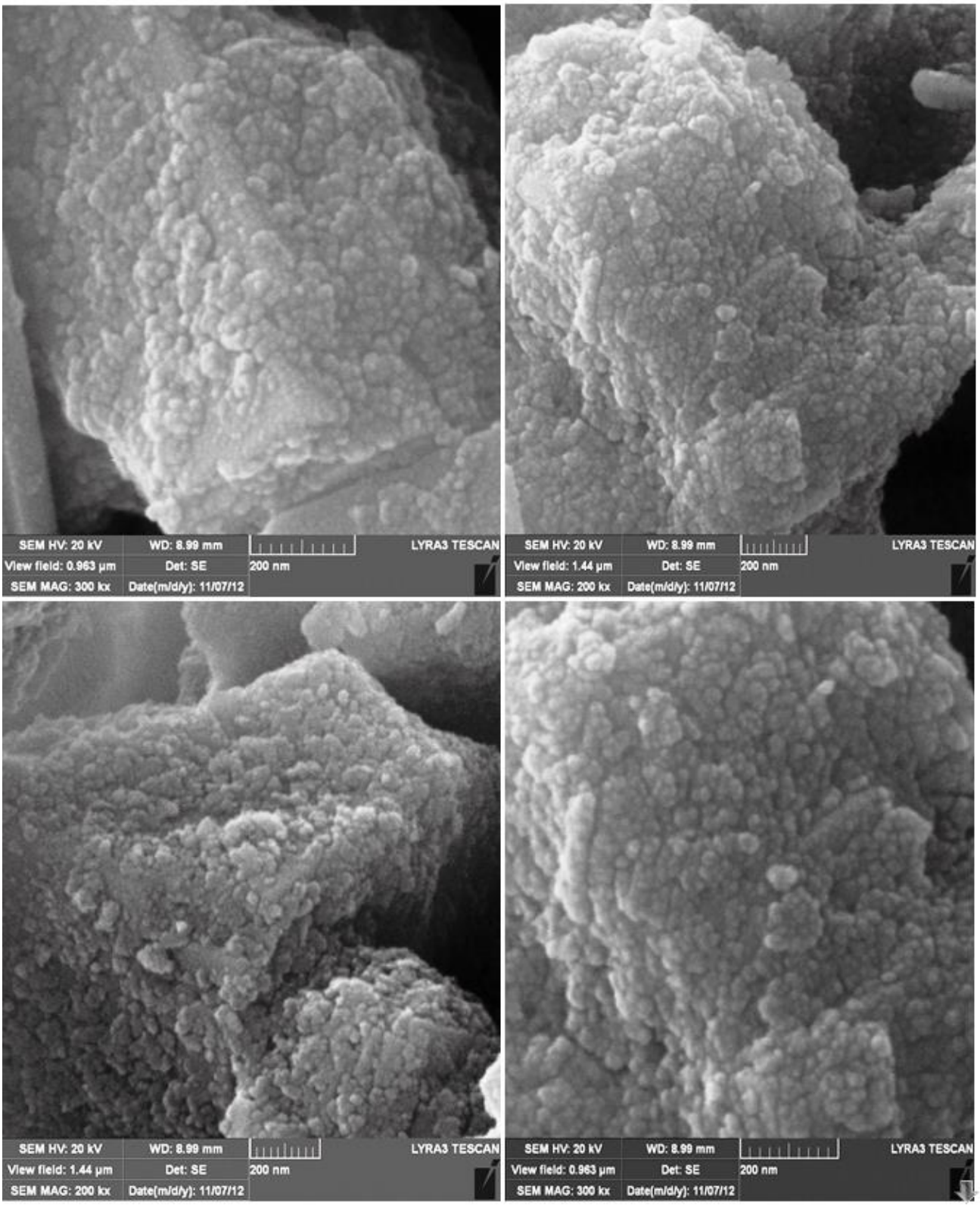

Figure 5.11 : SEM images of WO_3-C

5.1.1.5 X-ray photoelectron spectroscopy

WO_3-A and WO_3-B were analyzed by X-ray photoelectron spectroscopy (XPS) to determine the exact oxidation state of tungsten and to describe oxygen binding with hydrogen. First, we will discuss the XPS to determine the exact oxidation state of tungsten. Figure 5.12 shows the XPS fitting of tungsten in WO_3-A prepared in presence of hydrochloric acid. The blue spectra correspond to W 4f 7/2 (the bigger peak at ≈35-36) and W 4f 5/2 of W^{6+}, while the pink spectrum correspond to W 4f of W^{5+}. The integration of the spectra shows that the ratio (W^{6+}: W^{5+}) is (95.65: 4.35) indicating that WO_3-A is most probably $WO_{2.978}$. Figure 5.13 shows the XPS fitting of tungsten in WO_3-B. As can be observed form the figure, there is no peak corresponding to W^{5+} confirming that W^{5+} didn't form during the preparation of WO_3-B in presence of oxalic acid. This may prove that no partial reduction occurred under such conditions [63].

Second, we will discuss the XPS to describe oxygen binding. As shown in figure 5.14, there are two types of oxygen bonding in WO_3-A. The blue spectrum at 530.6 eV corresponds to O^{2-} specie, which represents the majority of oxygen while the pink spectrum at 531.9 eV corresponds to O^- specie. Thus, the ratio of O^-/ O^{2-} was found to be 0.15. Figure 5.15 shows the XPS fitting of oxygen in WO_3-B. The blue spectrum at 530.3 eV corresponds to O^{2-} specie; the orange spectrum at 531.1 eV corresponds to OH specie and the pink spectrum at 531.8 eV corresponds to O^- specie. The ratio O^-/ O^{2-} is 0.5 while the ratio of OH/ O^{2-} is 0.4. Therefore, the number of bridging O atoms (W-O-W) and O atoms with double bonds (W=O) are higher in WO_3-A comparing with WO_3-B; and the number of W-OH groups are less in case of WO_3-A comparing with WO_3-B [64]. The binding energies were corrected for the charge shift using the C1s peak (BE= 284.7 eV) as a reference.

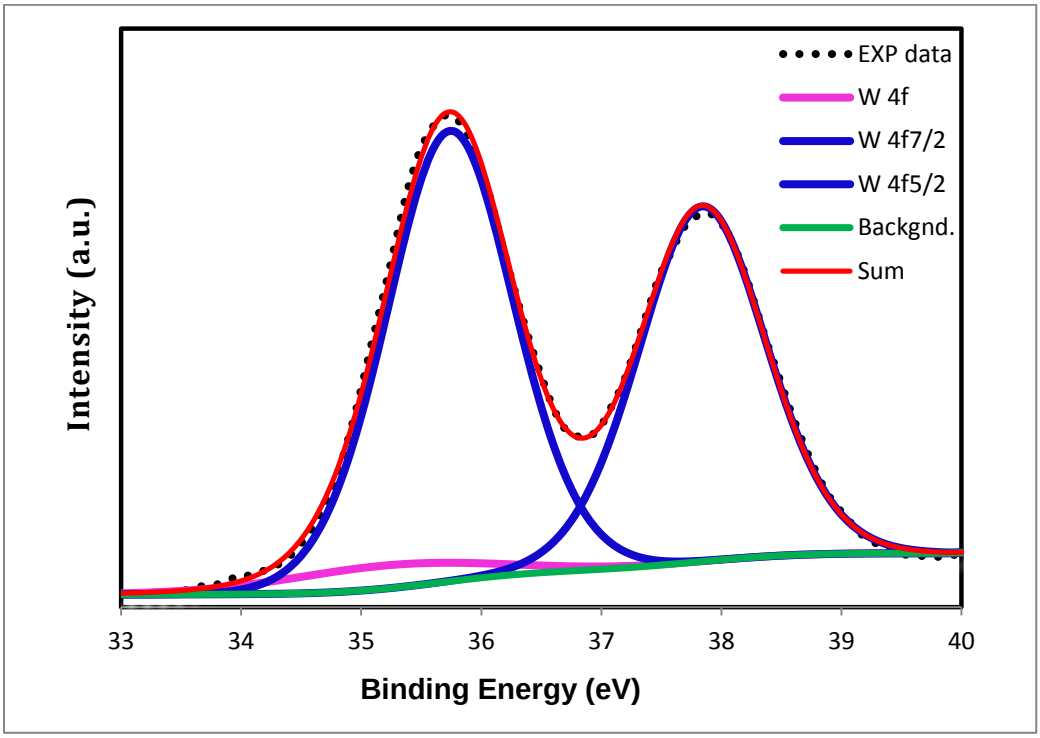

Figure 5.12 : W4f level XPS spectrum of WO_3-A

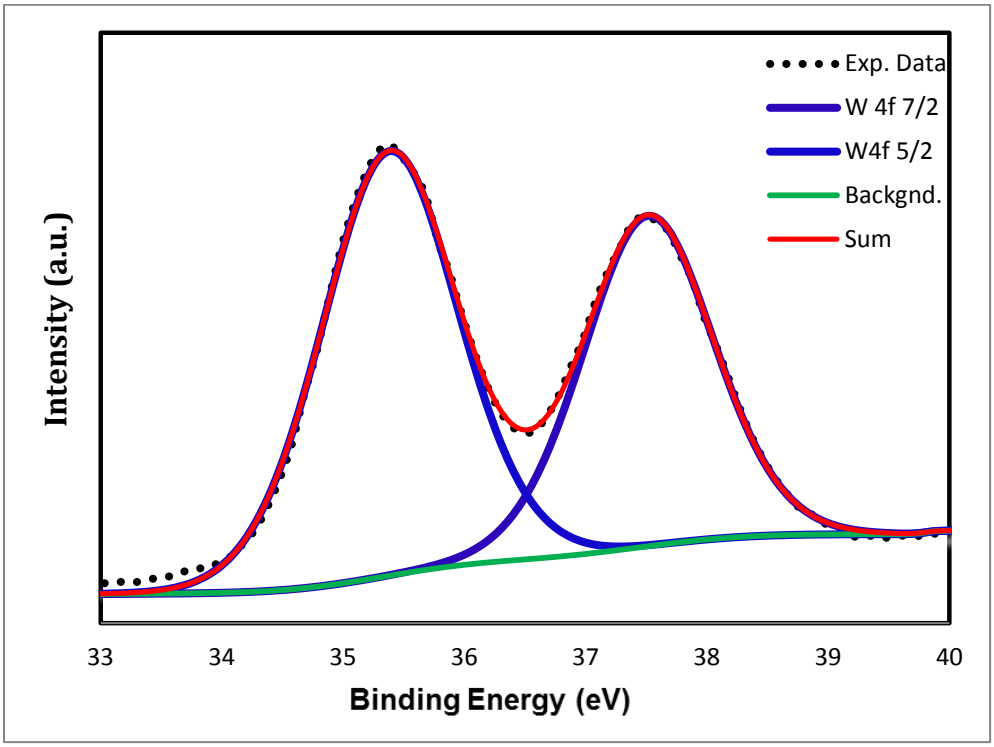

Figure 5.13 : W4f level XPS spectrum of WO_3-B

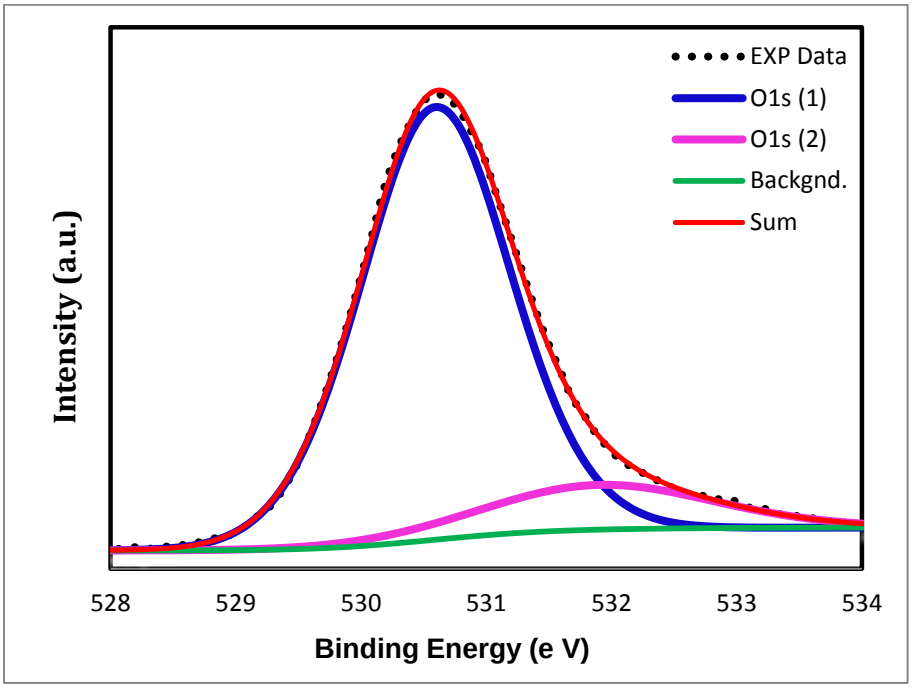

Figure 5.14 : O1s-level XPS-spectrum of WO_3-A

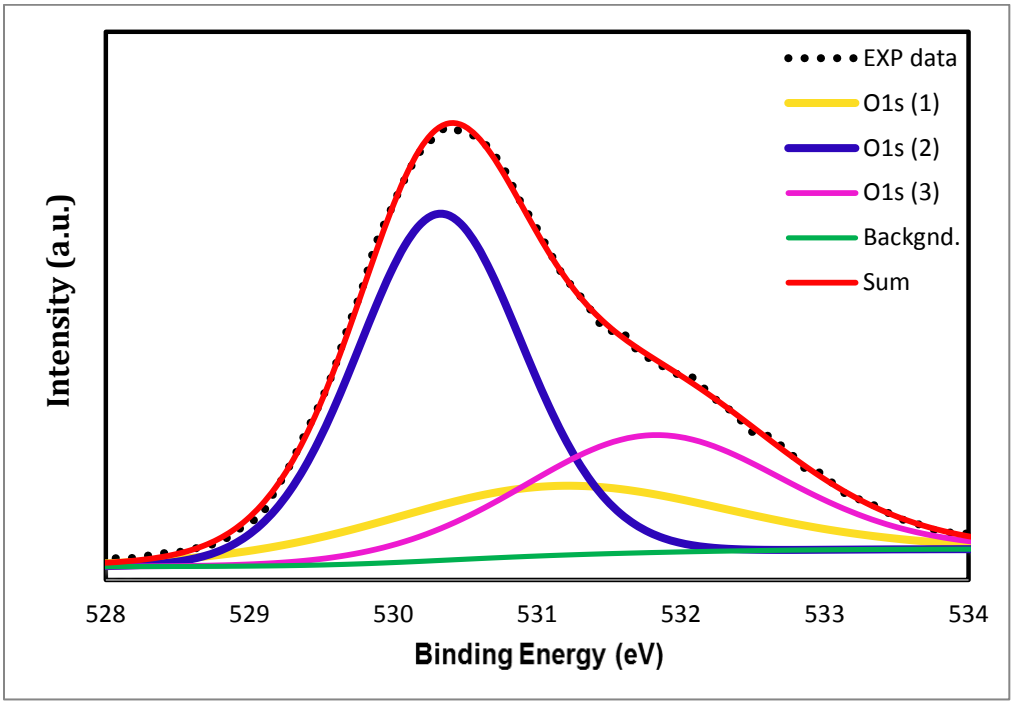

Figure 5.15 : O1s-level XPS-spectrum of WO_3-B

5.1.1.6 UV-Vis spectroscopy

WO_3-A and WO_3-B were noticed to have color difference. When WO_3-B is yellow just like bulk WO_3, WO_3-A has a blue color. Figure 5.16 shows the significant difference in UV-Vis spectroscopy of WO_3-A and WO_3-B. WO_3-A reflects the radiation more in visible spectrum and less in UV region. However, this difference in the optical properties could be one of the factors that create the photocatalytic activity differences between the synthesized tungsten oxides.

5.1.2 Characterization of Pt in Pt/WO_3 via TEM

Platinum nanoparticles on the surface of tungsten oxide were characterized by transmission electron microscopy. Figure 5.17 shows the TEM photograph of 2% Platinum/ WO_3-A. The photograph shows that the platinum crystals have the size of approximately 3 nanometers. ESD spectrum to this very spot in the photograph shows the platinum presence on its surface.

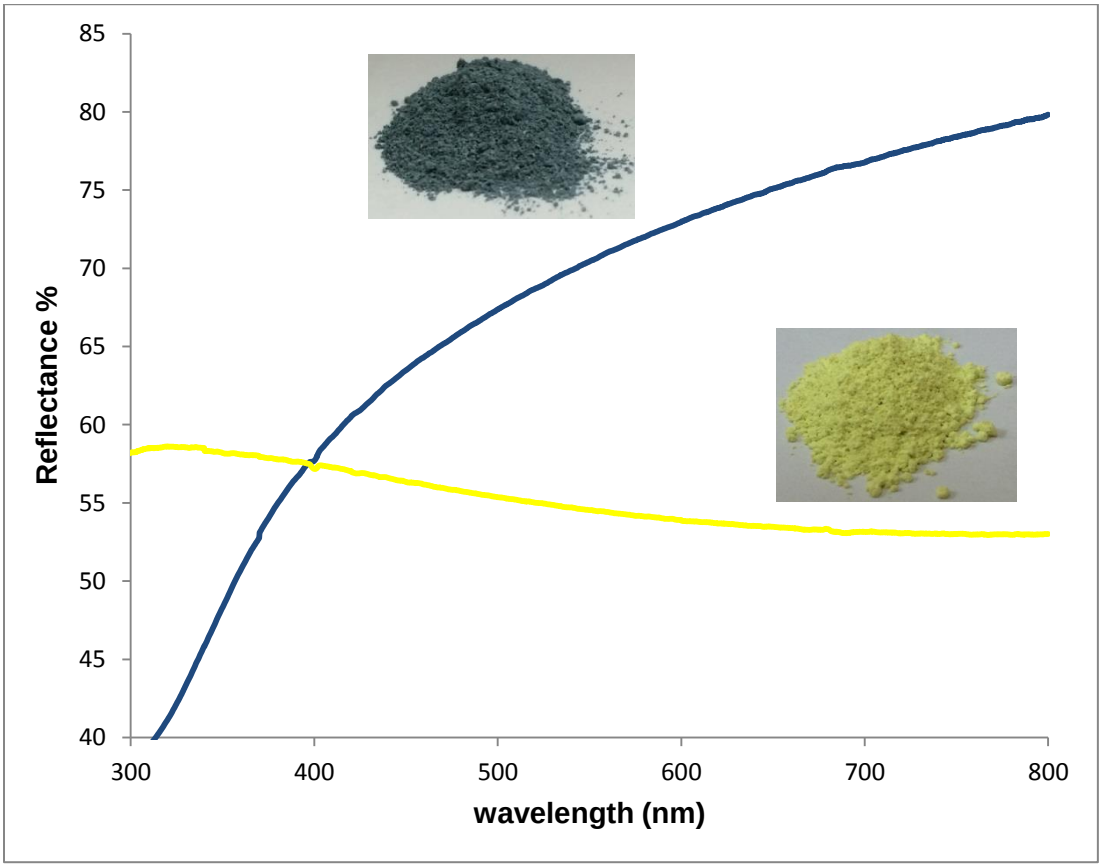

Figure 5.16 : UV-Vis spectroscope of WO_3-A (blue) and WO_3-B (yellow)

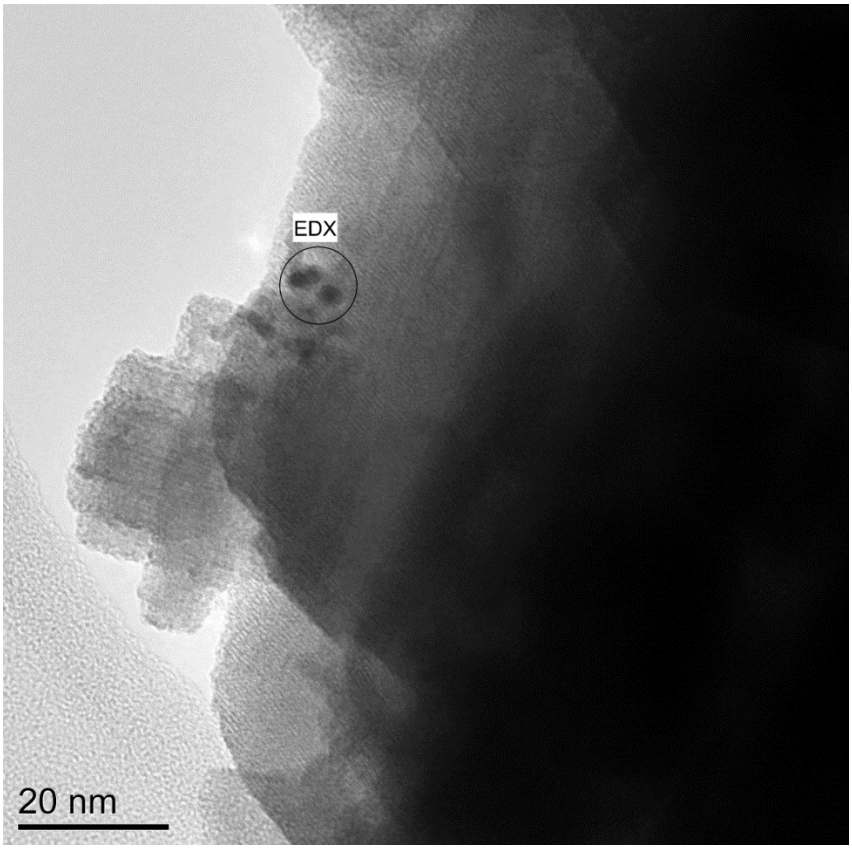

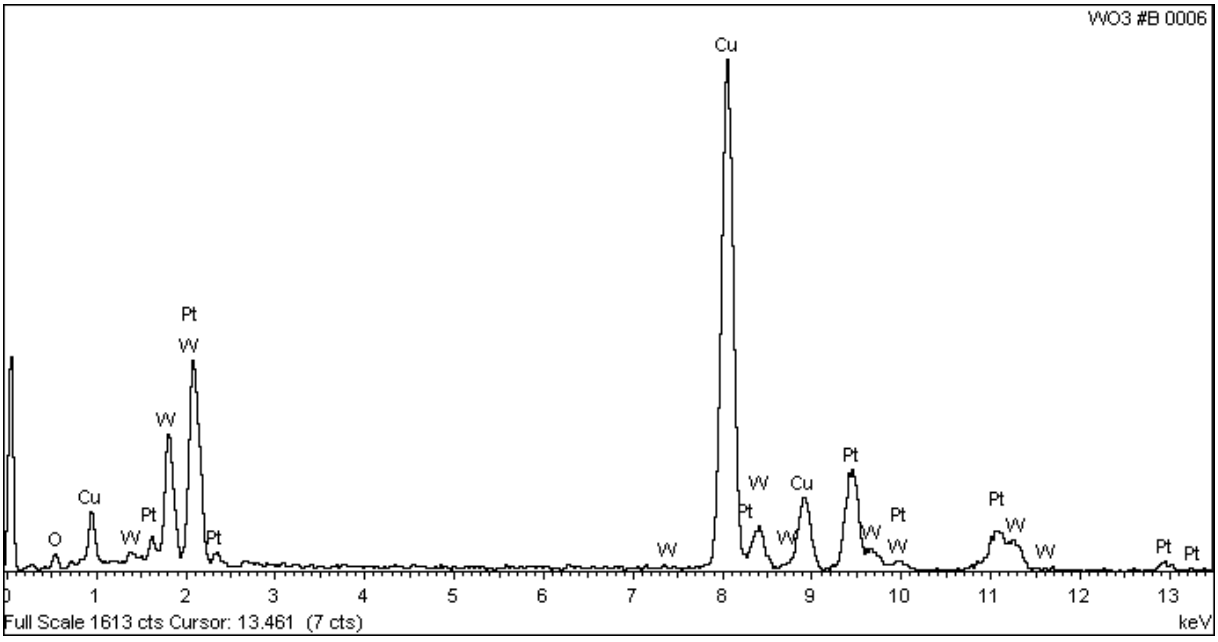

Figure 5.17 : TEM and EDX spectrum for Pt/WO_3

5.1.3 Characterization of graphene

5.1.3.1 Fourier transform infrared spectroscopy analysis

As mentioned, graphene was prepared by oxidation of graphite into graphite oxide, exfoliation of graphite oxide into graphene oxide by ultrasonicator, and then reduction of graphene oxide into graphene. Figure 5.18 shows FT-IR spectrum of graphite and graphite oxide. Graphite spectrum doesn't show any oxygen-containing functionality (e.g. O-H and C=O). However, graphite oxide spectrum shows many oxygen-containing functionalities like O-H bond at 3400 cm^{-1} and C=O bond at 1600 cm^{-1} proving that oxidation reaction took place on graphite. Figure 5.19 compares between FT-IR spectra of graphene oxide and graphene. The spectra show that most of the oxygen-containing functionalities were reduced in case of graphene proving that reduction reaction took place on graphene oxide.

5.1.3.2 Raman spectrometry analysis

To differentiate between graphene, multilayer graphene and graphite, Raman spectroscopy was used. The number of layers can be derived from the ratio of peak intensities of G peak (1580 cm^{-1}) and 2D peak (2690 cm^{-1}) I_{2D}/I_G. The I_{2D}/I_G value of ~2 indicates monolayer graphene. 2> I_{2D}/I_G >1 indicates bilayer while I_{2D}/I_G <1 indicates multilayers graphene [65-67].

Figure 5.20 shows Raman spectrum of the prepared graphene, and it demonstrates the presence of G and 2D peaks with I_{2D}/I_G = 2.05 which indicates that the prepared material could be monolayer graphene.

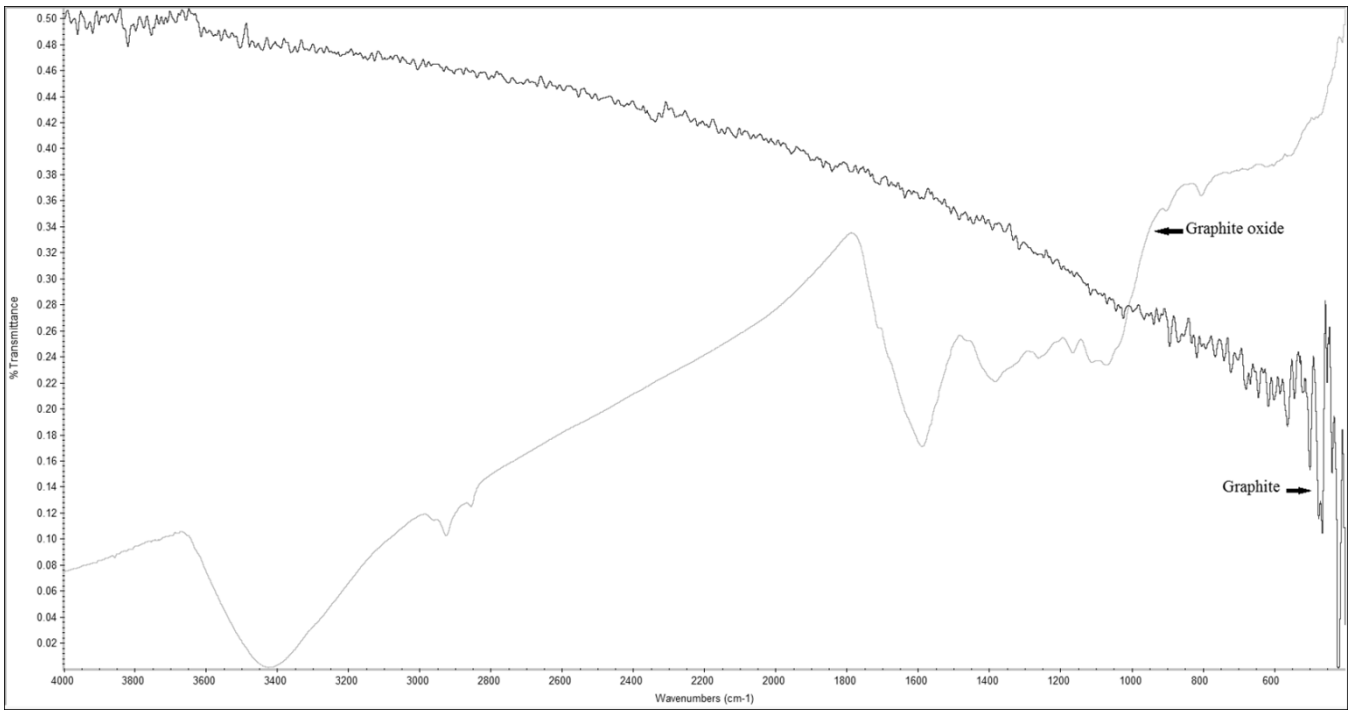

Figure 5.18 : FT-IR of graphite and graphite oxide

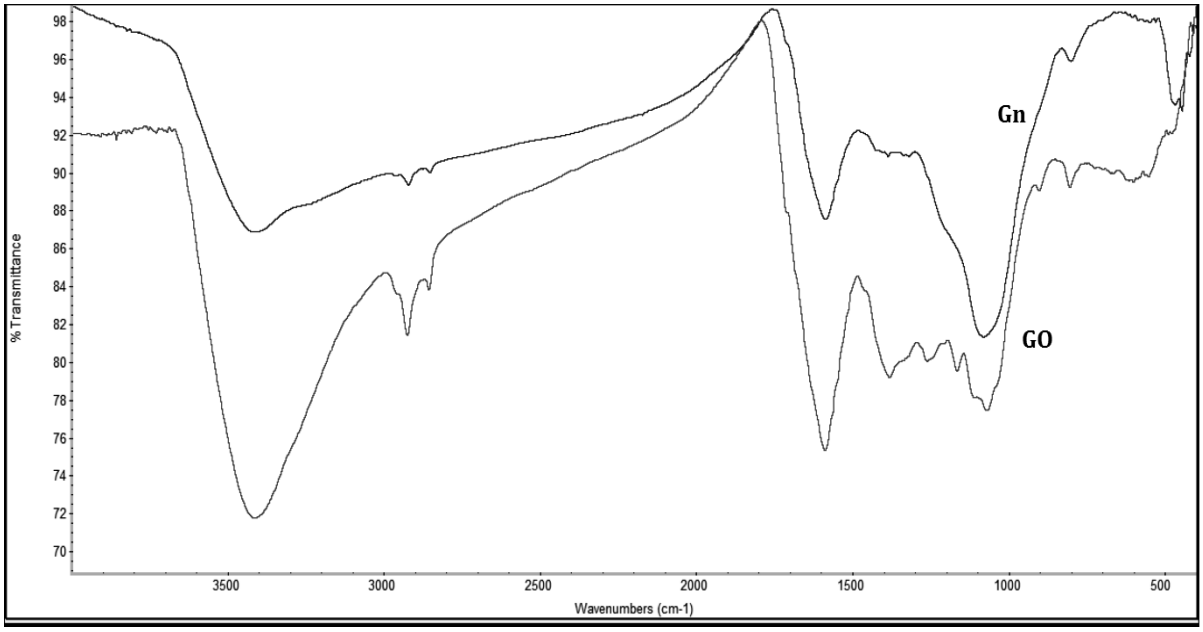

Figure 5.19 : FT-IR of graphene oxide and graphene

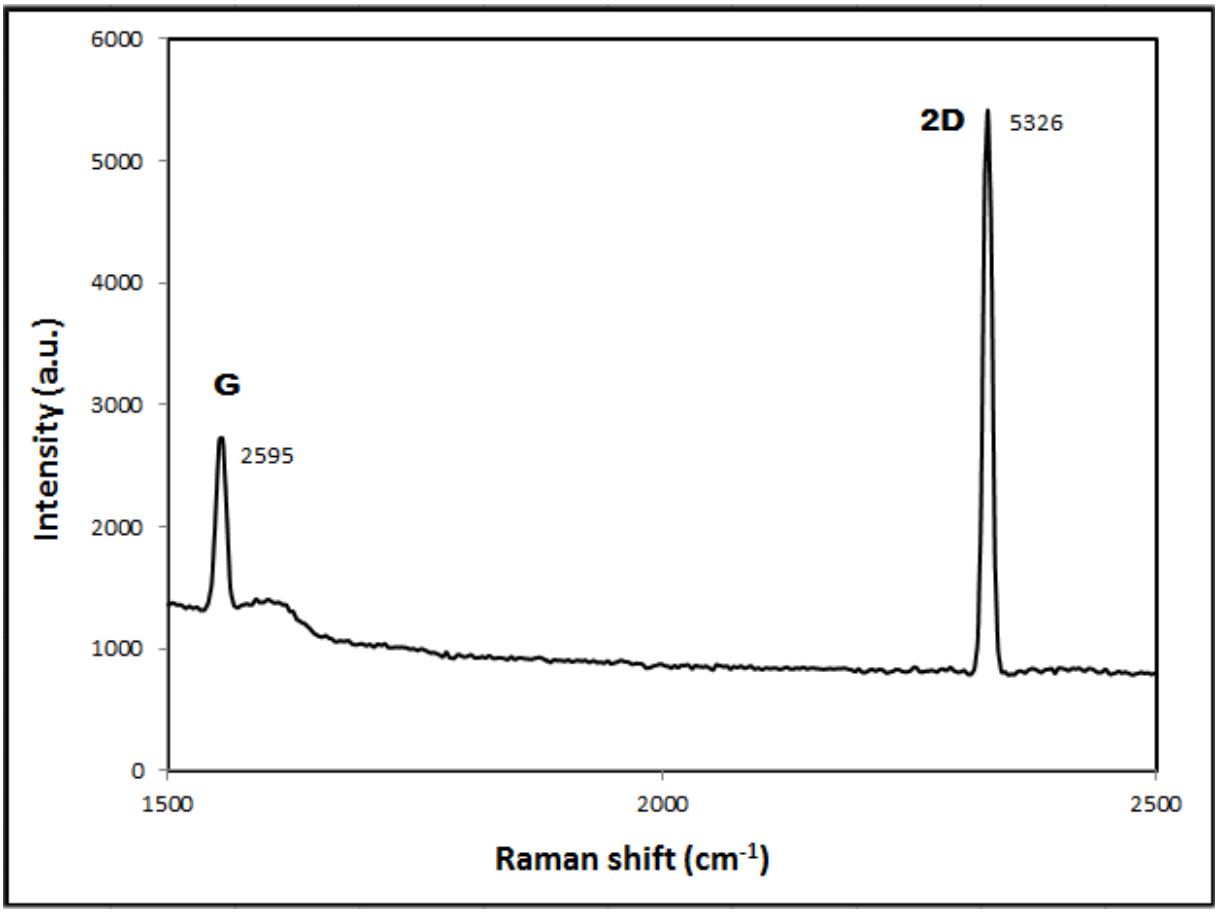

Figure 5.20 : Raman spectrum of the prepared Graphene

5.1.4 Characterization of WO_3/Gn composite

5.1.4.1 Field emission scanning electron microscope analysis

WO_3/Gn composite was characterized by field emission electron microscope. Figure 5.21 shows the FESEM photograph of WO_3-A/ graphene with graphene content of 5%. Tungsten oxide crystals can easily be observed in the photograph while graphene presence can be confirmed by the comparison between secondary electrons (SE) and Back-scattered electrons (BSE) (SE left and BSE right). BSE signal is strongly related to the atomic number meaning that tungsten has high BSE signal while carbon with its small atomic number have small BSE signal.

5.1.4.2 Energy dispersive X-ray analysis

EDS (energy dispersive X-ray spectroscopy) was performed on WO_3-A/Gn to identify the elements and their ratio and their distribution in the composite. Figure 5.22 shows EDS spectrum of WO_3/Gn with 5% graphene content. The spectrum confirms the presence of tungsten, oxygen, and carbon in the composite. Figure 5.23 shows the ratios of the elements in different spots of the composite. The ratio of oxygen to tungsten is 3/1 while carbon appears to be higher than the content in the composition. This can be explained probably due to the adsorption of some carbon-containing gases. Figure 5.24 shows the distribution of the elements in the composition, and it demonstrates good distribution of all elements in it.

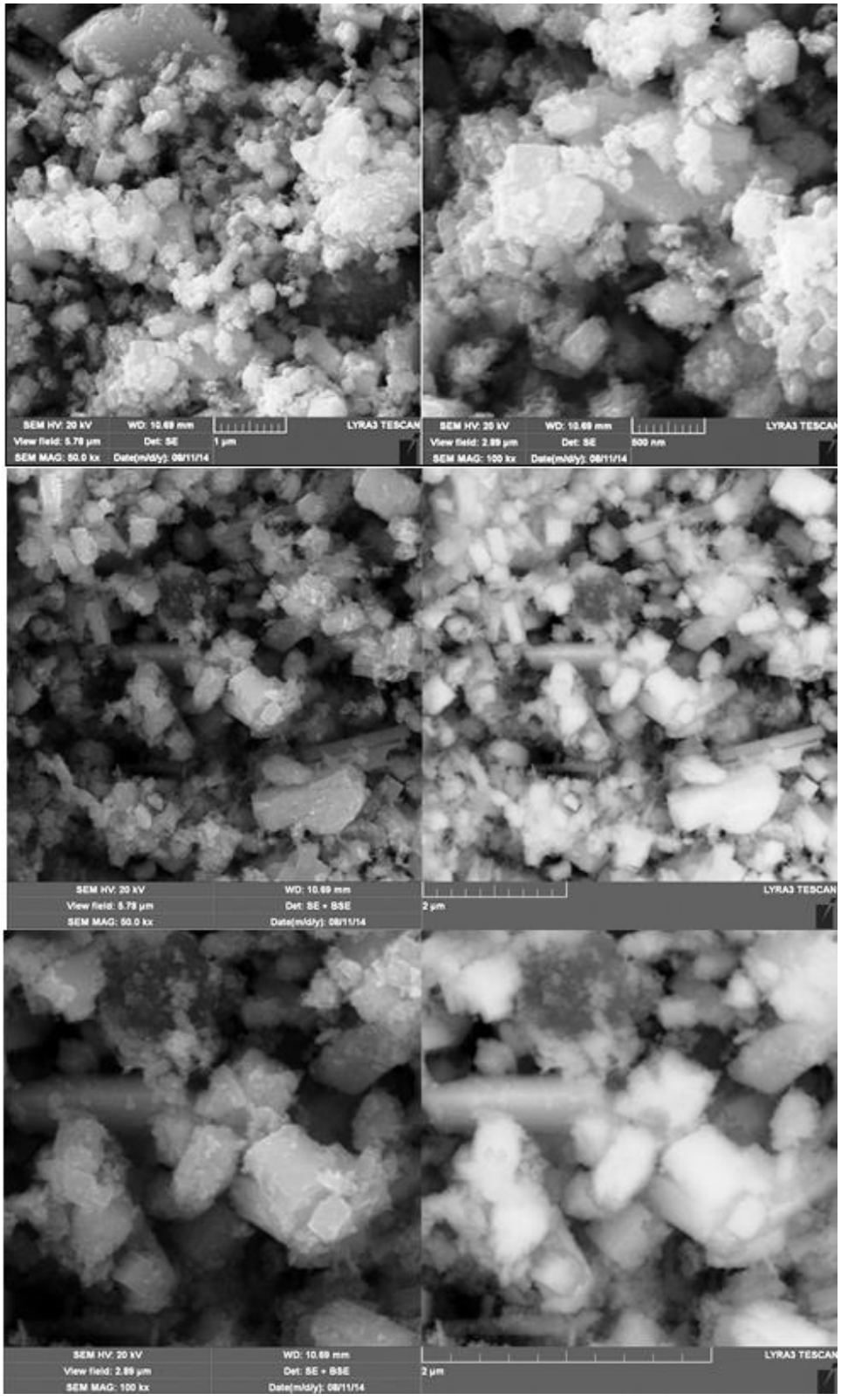

Figure 5.21 : SEM images of WO_3/Gn

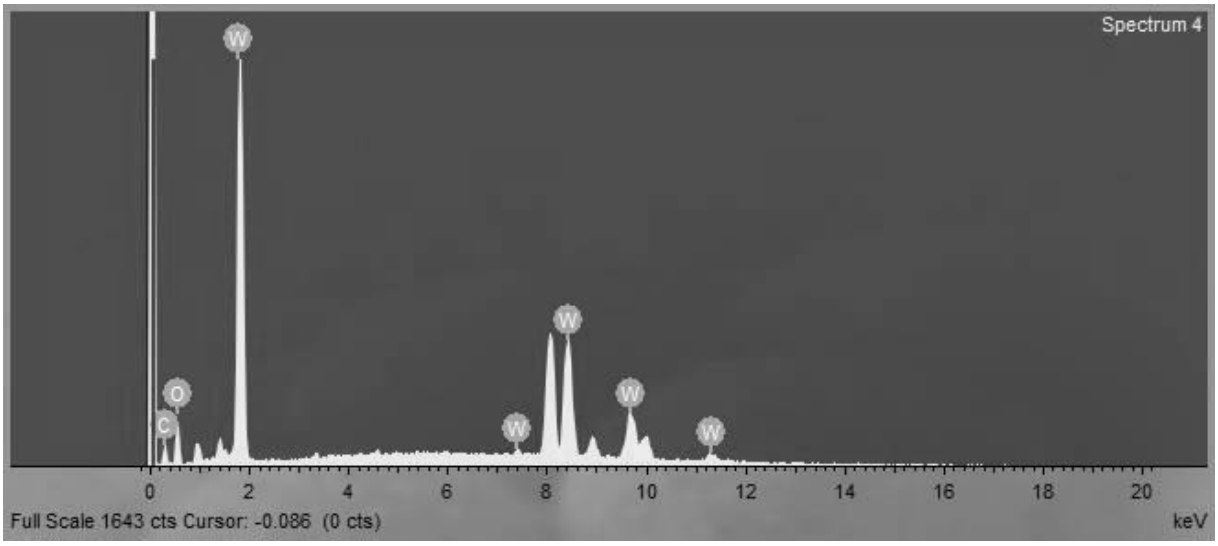

Figure 5.22 : EDS spectrum of WO_3/Gn

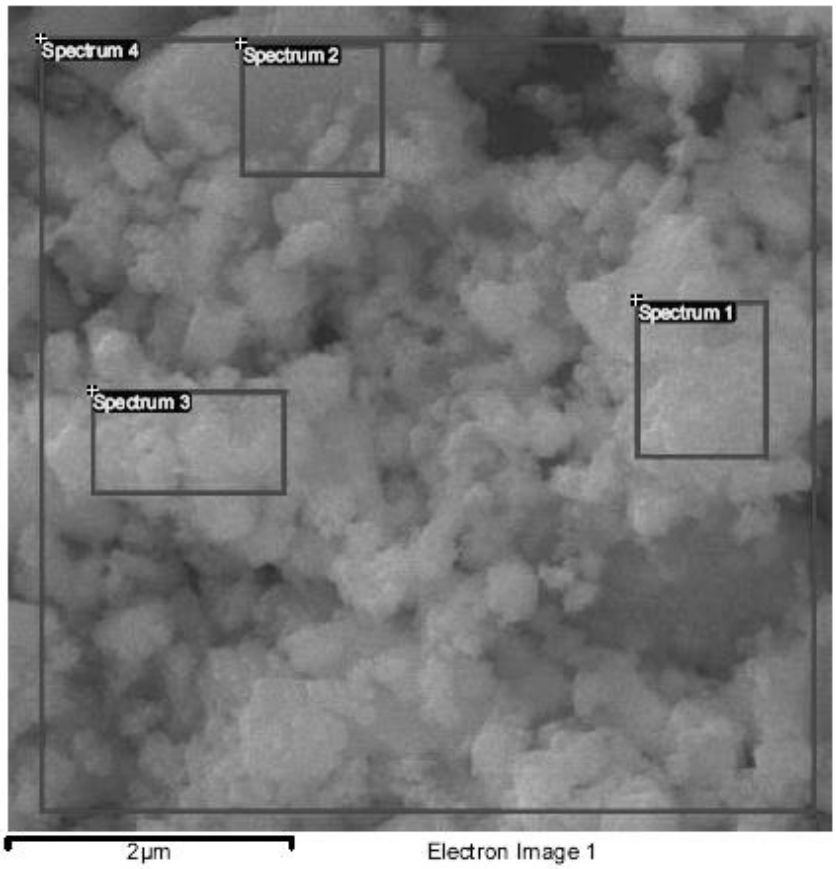

Processing option : All elements analysed (Normalised)

Spectrum	In stats.	C	O	W	Total
Spectrum 1	Yes	23.08	21.05	55.87	100.00
Spectrum 2	Yes	9.35	9.86	80.78	100.00
Spectrum 3	Yes	13.31	22.29	64.40	100.00
Spectrum 4	Yes	14.02	16.53	69.45	100.00
Mean		14.94	17.43	67.63	100.00
Std. deviation		5.80	5.62	10.41	
Max.		23.08	22.29	80.78	
Min.		9.35	9.86	55.87	

All results in weight%

Figure 5.23 : Elements ratios in WO_3/Gn

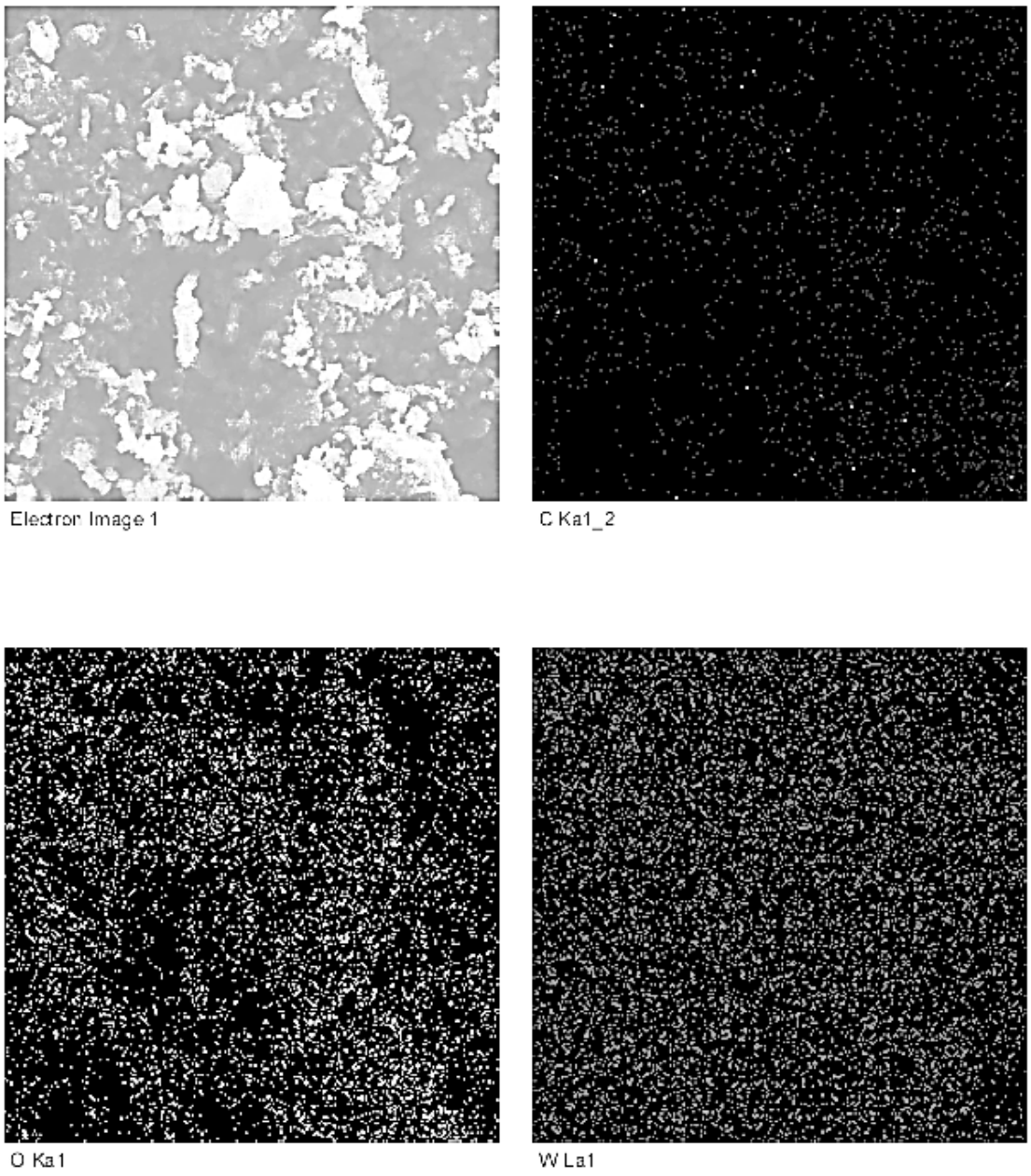

Figure 5.24 : The distribution of C, O and W in WO_3/Gn

5.1.4.3 Fourier transform infrared spectroscope analysis

To confirm the synthesis of the composite, comparison between their FT-IR spectra were conducted. Figure 5.25 shows FT-IR spectra of WO_3-A/Gn composite and WO_3-A/Gn mixture, the spectrum shows partial reduction of C=O at 1600 cm^{-1} due to the hydrothermal treatment of graphene and WO_3-A. The spectrum of WO_3-A /Gn composite shows peaks at ~ 830 cm^{-1} and ~ 3600 cm^{-1} that don't exist in the mixture, probably due to the formation of bonds between WO_3 and graphene.

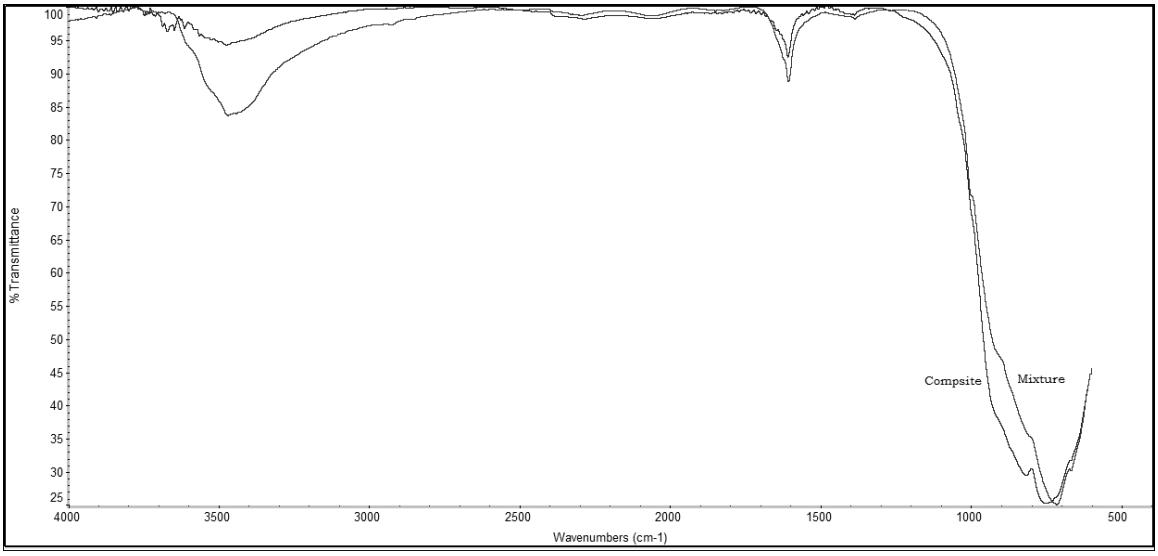

Figure 5.25 : FT-IR of WO_3/Gn composite and WO_3/Gn mixture

5.2 Photocatalytic application

5.2.1 Effect of different nanostructured WO_3

Three forms of nanostructured tungsten oxide were tested, WO_3-A (prepared in the presence of hydrochloric acid), WO_3-B (prepared in the presence of oxalic acid) and WO_3-C (prepared in the presence of oxalic acid and hydrochloric acid). Figure 5.26 shows that all nanostructured tungsten oxides have higher conversion of alcohol than bulk-WO_3. This is probably due to the increase in the surface area and consequently an increase in the speed of the reaction. WO_3-B has surface area higher than the surface area of WO_3-A though WO_3-A has better conversion activity (5%) compared to WO_3-B (2%), as shown in figure 5.21. This can be explained by partial reduction of WO_3-A during the hydrothermal synthesis as confirmed by XPS by the formation of W^{5+} species in case of WO_3-A. This was observed by the color of WO_3-A turning from yellow into blue during the synthesis [61]. It is well known that when W^{5+} species formed in the lattice, a strong absorption of the visible light in 500−800 nm range occurred [68], leading to an enhancement in the photocatalytic activity. Moreover, Oxygen vacancies in WO_3-A trap electrons to be stored, and consequently preventing them from recombination with holes in the valence band (VB) [69]. WO_3-A was selected as an optimum tungsten oxide for the research purpose in this thesis.

5.2.2 Effect of irradiation and catalyst absence

To prove the importance of the catalyst and the visible light radiation, the reaction was studied in the absence of the catalyst and in the absence of the irradiation. No significant conversion of alcohol has been detected in both cases, which mean that the presence of both the catalyst and irradiation are conditional for the reaction to take place.

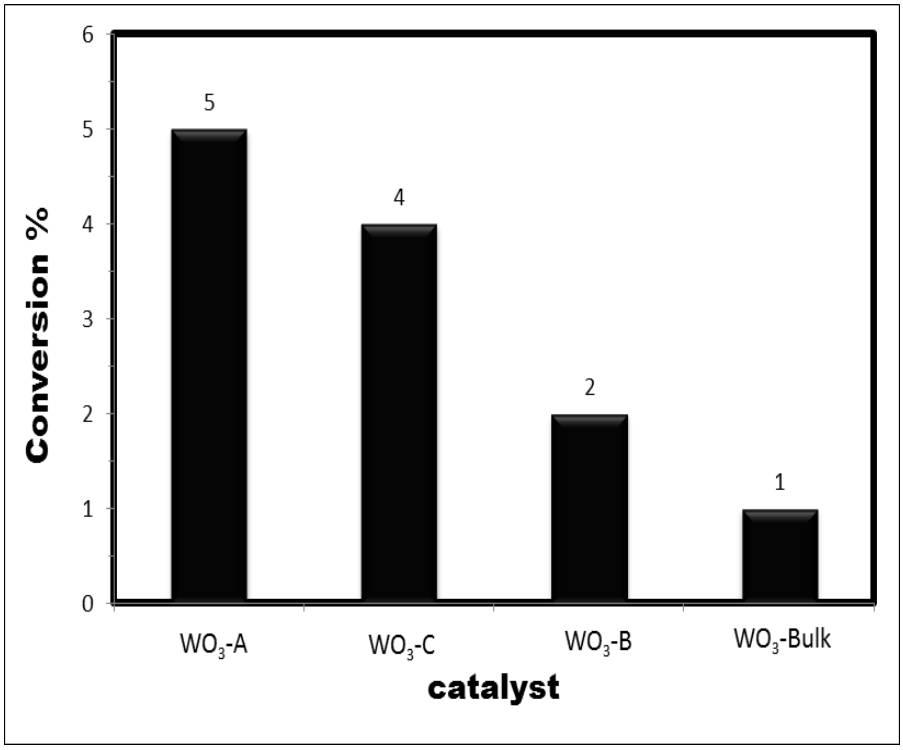

Figure 5.26 : Effect of different nanostructured WO_3

5.2.3 Effect of the catalyst concentration

At first, increasing the concentration of the catalysts increases the reaction conversion because of the increase in the interaction area between the catalyst and the reactant. Then the catalysts start shielding the reactant from the irradiation which leads to decreasing in the reaction conversion. Figure 5.27 shows that increasing the concentration of WO_3/Pt lead to an increase in the conversion of alcohol. However, at higher concentration, the increasing of the conversion of alcohol decelerated.

For commercial and environmental purposes, decreasing the amount of the catalyst is highly desirable, that is why instead of 3 gram/ letter, 2 gram/ letter was selected to be an optimum catalyst concentration for this study.

5.2.4 Effect of alcohol concentration

Generally, in photocatalysis, increasing the concentration of the reactant causes higher possibility of the reaction to take place and that lead to faster and more conversion reaction. However, after specific extent, increasing the concentration of the reactant decreases the conversion due to an increase in the concentration of the product, which gets adsorbed on the catalyst surface, preventing the catalyst to adsorb the reactant and consequently, inhabiting the reaction.

Figure 5.28 shows the effect of alcohol concentration on the conversion percentage when different concentrations of benzyl alcohol (0.5, 1, 1.5 and 2) mmol /L were studied. The best concentration for this reaction found to be 1.5 mmol /L.

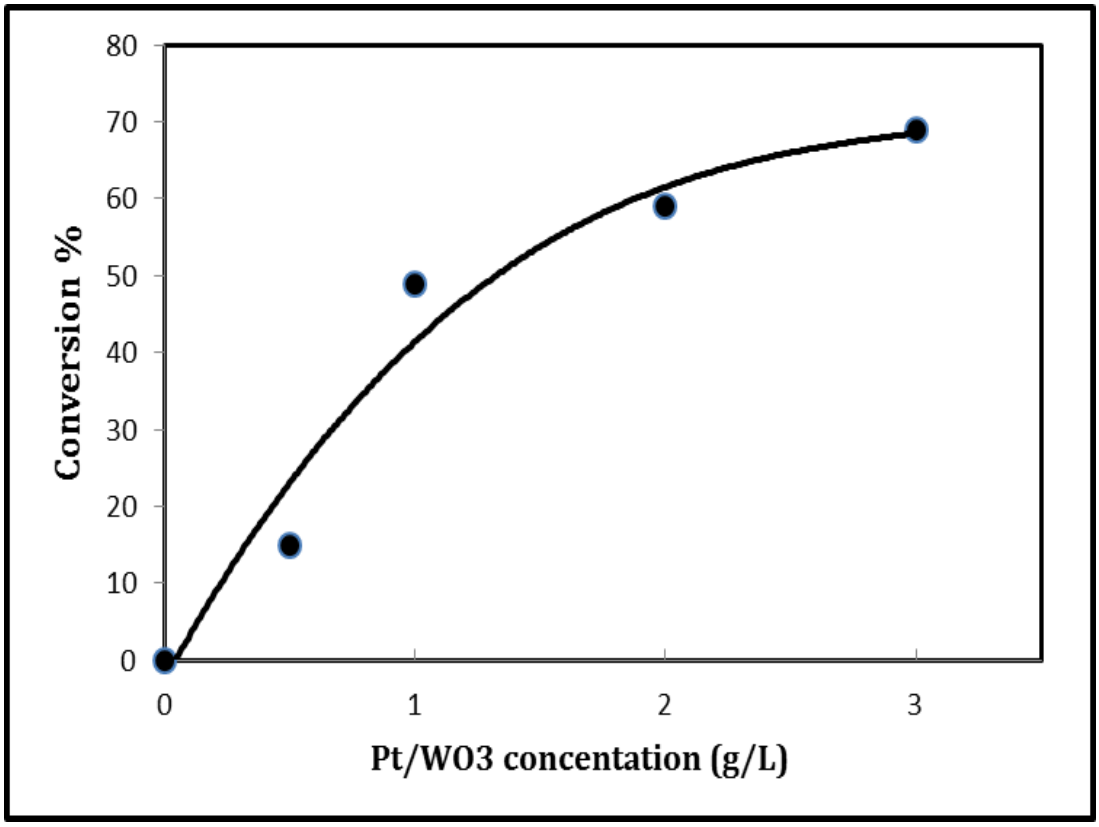

Figure 5.27 : Effect of the catalyst concentration

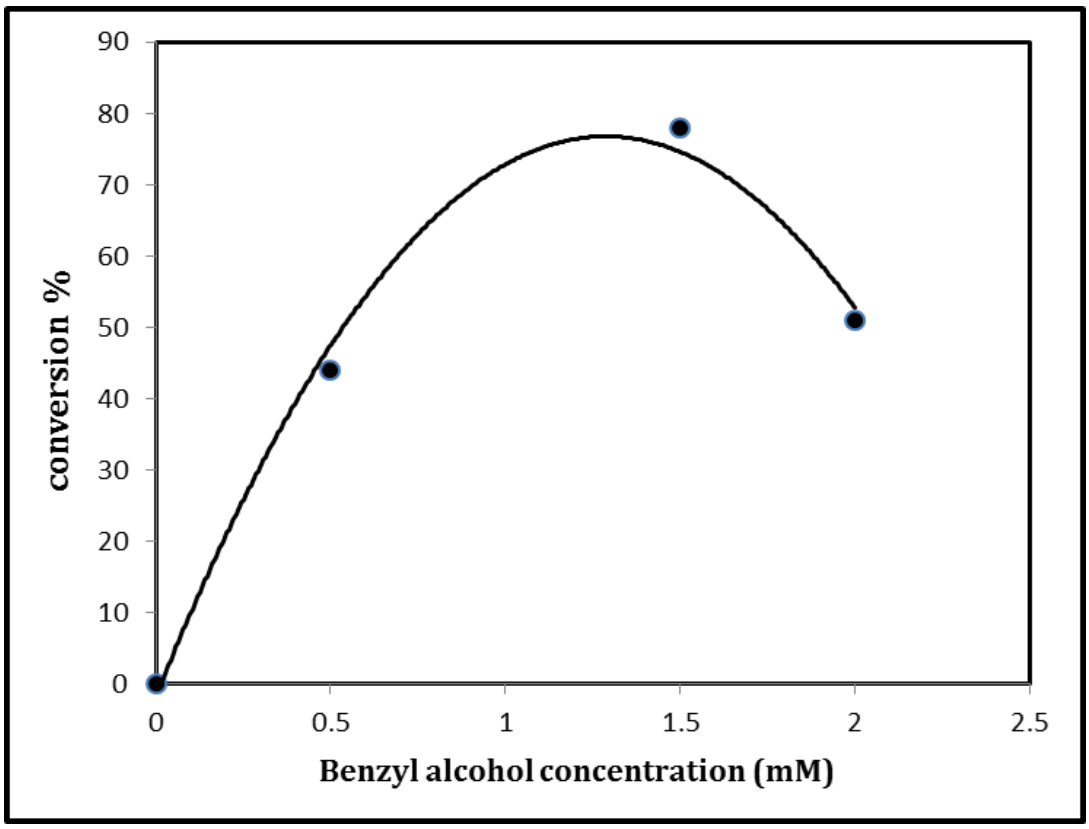

Figure 5.28 : Effect of alcohol concentration

5.2.5 Effect of Pt content

As mentioned previously, platinum nanoparticles increases the photocatalytic activity by captivating electrons, decreasing its recombination with holes and consequently making the holes more available. Figure 5.29 shows that at first, when platinum content in the catalyst increases the photocatalytic activity increases. This is because more electrons were captivated by platinum. After that, the photocatalytic activity starts to decrease because of decreasing the surface of the interaction between the tungsten oxide and the radiation. The optimum platinum content in the composite is 2 percent.

5.2.6 Effect of graphene content

As mentioned in the introduction, graphene increase the photocatalytic activity of the catalyst by preventing the agglomeration of the semiconductor and by its electrons acceptor properties. However, absorbing the radiation by graphene may decrease the photocatalytic activity. Thus competitive factors lead to a necessity of investigating the optimum content of the graphene in the composite. Figure 5.30 shows conversion percent using different graphene content (0.5, 1, 2.5and 5%). The photocatalytic activity increases in case of small content of graphene, but it decreases when this content start to increase and even becomes catalyst inhibitor at 5%. Therefore, the optimum graphene content was observed to be 0.5 percent.

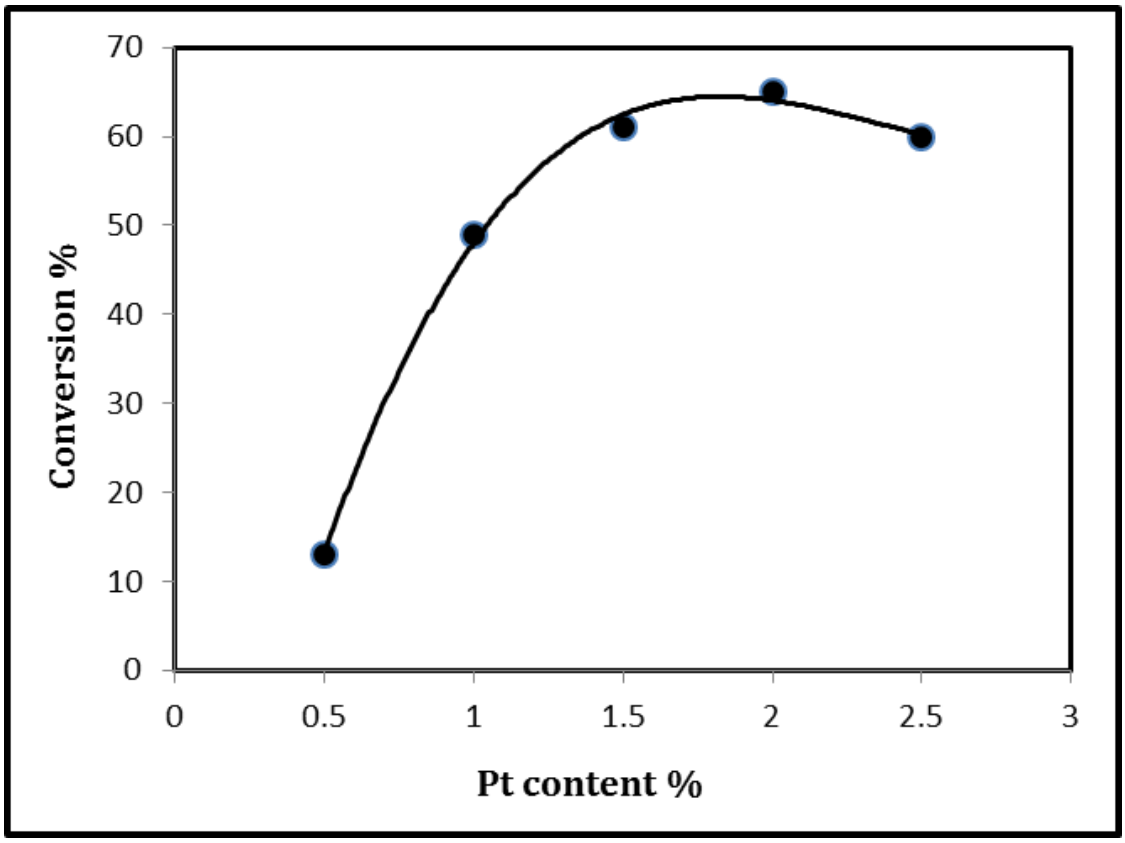

Figure 5.29 : Effect of Pt content

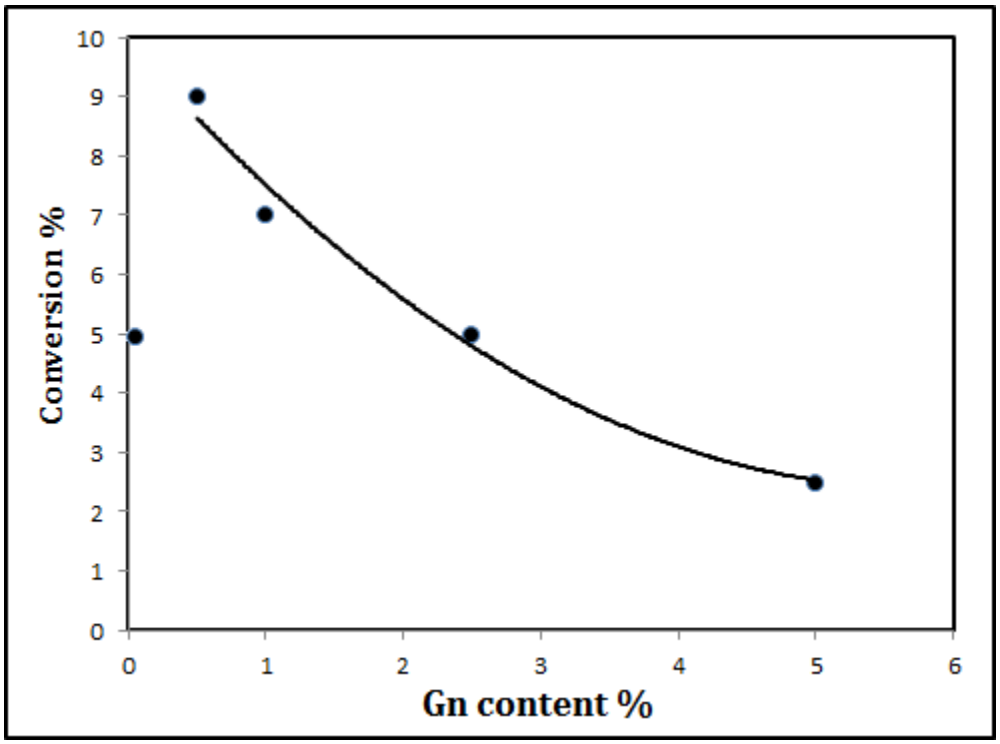

Figure 5.30 : Effect of graphene content

5.2.7 WO_3/Gn nanocomposite vs. WO_3/Gn mixture

Figure 5.31 illustrates that WO_3/Gn nanocomposite has higher photocatalytic activity compared to mechanical mixture of WO_3/Gn and that because graphene acts differently. In the mixture, graphene can prevent agglomeration, while in the nanocomposite; it can also be an electron acceptor, which means less holes- electrons recombination and more photocatalytic reactivity toward oxidation reactions.

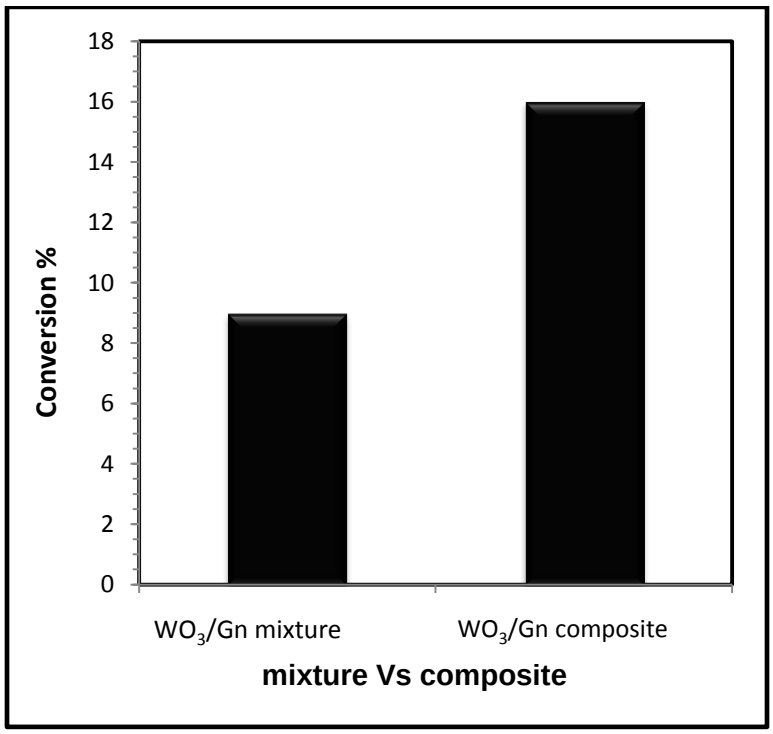

Figure 5.31 : WO_3/Gn composite VS. WO_3/Gn mixture

5.2.8 Effect of different alcohols

The photocatalytic oxidation of benzyl alcohol, 4-methoxy benzyl alcohol and cinnamyl alcohol were studied under the optimal conditions. Figure 5.32 indicates that Pt/WO_3 photocatalytic activity was the highest in case of cinnamyl alcohol with conversion of 84%, then benzyl alcohol with 78% and 4-methoxy benzyl alcohol with 74%, and that probably because of the difference between those alcohols in the chemical structures. Hydroxyl group is adjacent to a double bond in cinnamyl alcohol. However, it is adjacent to a benzene ring that could make the alcohol group sterically hindered in both benzyl alcohol and 4-methoxy benzyl alcohol. The methoxy group in 4-methoxy benzyl alcohol obviously decreased the photocatalytic activity probably due to its electron donating properties.

Similarly, figure 5.32 shows that $Pt/WO_3/Gn$ photocatalytic activity has the same order with higher conversions values (90% in cinnamyl alcohol, 83% in benzyl alcohol and 80% in 4-methoxy benzyl alcohol). Table 5.1 shows the chemical structure of the studied alcohols.

5.2.9 Effect of different catalysts

Nanostructured tungsten oxide was modified by adding platinum nanoparticles and/or graphene. Figure 5.32 compares between the photocatalytic activity of Pt/WO_3, WO_3/Gn and $Pt/WO_3/Gn$. It shows that the photocatalytic activity of Pt/WO_3 is much better compared to WO_3/Gn. It also shows that the best catalyst is $Pt/WO_3/Gn$ for all the studied alcohols.

Table 5.1 : The chemical structure of the studied alcohols

Alcohol name	**Alcohol structure**
Benzyl alcohol	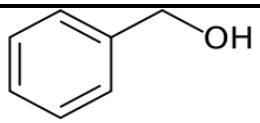
4-methoxy benzyl alcohol	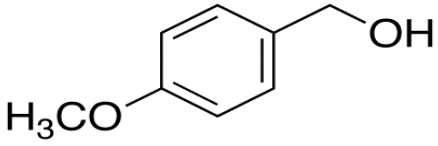
Cinnamyl alcohol	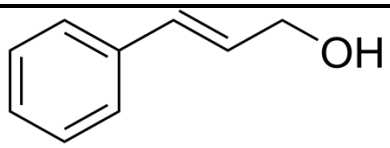

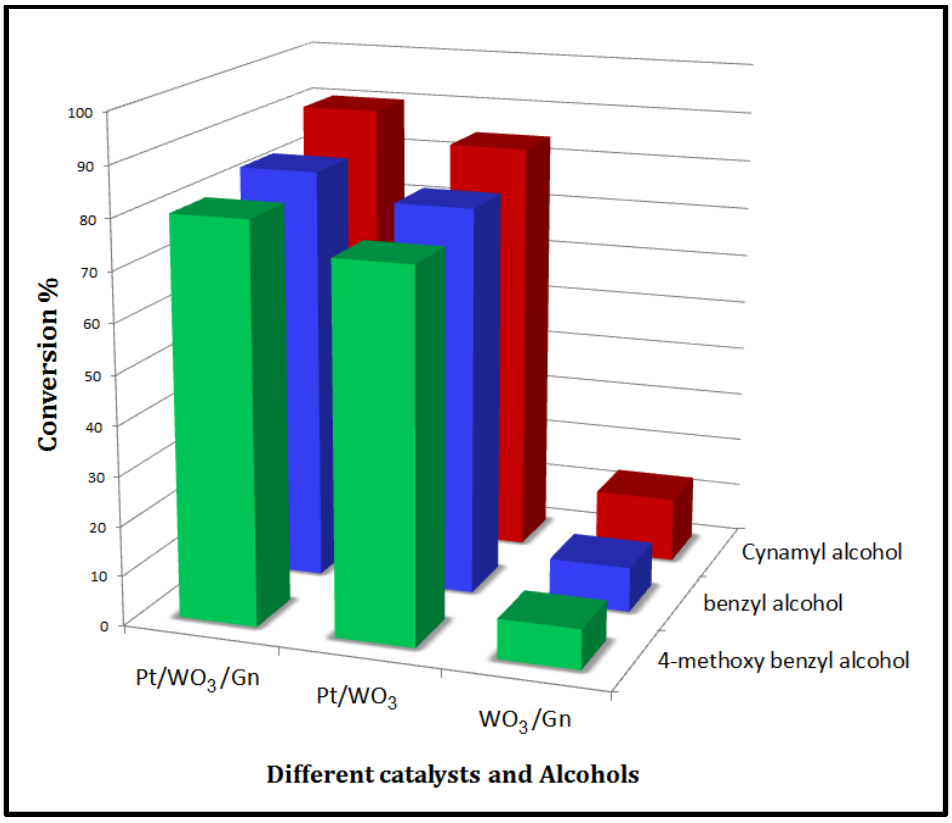

Figure 5.32 : Effect of different catalysts and alcohols

5.2.10 Reaction mechanism

Photocatalytic oxidation of benzyl alcohol occurs by eliminating two hydrogen atoms from the molecule, while the elimination of hydrogen adjacent to carbon in the first stage is most likely due to the thermodynamical stability of such species by resonance compared to the hydrogen adjacent to oxygen elimination case [70].

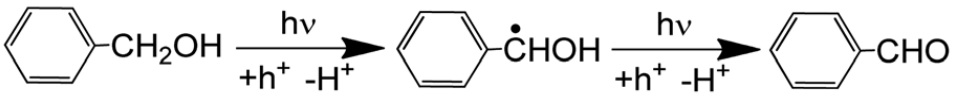

Figure 5.33 shows a representation of the reaction mechanism under sunlight radiation. The representation indicates that both platinum nanoparticles and graphene improves the photocatalytic activity of tungsten oxide by reducing the electron-hole recombination. However, platinum nanoparticles can also improve the photocatalytic activity by catalyzing hydrogen reduction on its surface which is probably the reason of the superiority of platinum nanoparticles over graphene in improving the photocatalytic activity of tungsten oxide.

To study the role of the oxygen gas in the mechanism of the photocatalytic reaction, O_2 and N_2 were bubbled during the reaction. Figure 5.34 depicts the comparison between the bubbling of O_2, N_2 and working normally under air. Oxygen bubbling increases the conversion of alcohol very slightly due probably to the aerobic oxidation of alcohols.

Nitrogen bubbling was performed to study the effect of O_2 absence. Figure 5.34 shows that nitrogen bubbling slightly decreases the photocatalytic activity which means that oxygen is not part of the reaction mechanism. Instead, oxidation could take place on the surface of the catalyst.

The selectivity of the reaction justified by the fact that oxidation of alcohol to aldehyde is oxidative dehydrogenation reaction which means no oxygen atoms is added to the molecule. However, other competitive reaction like further oxidation of aldehyde to carboxylic acid or oxidation of benzene ring requires adding of oxygen atoms which is not possible under the prepared catalyst due to the fact that O_2 can't be reduced on the catalyst surface.

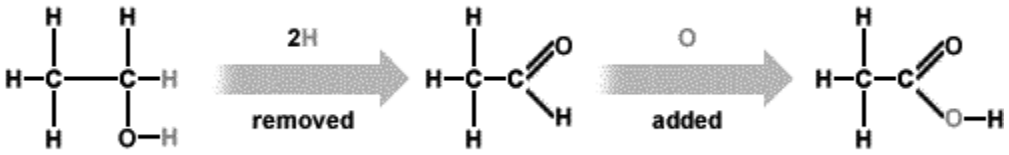

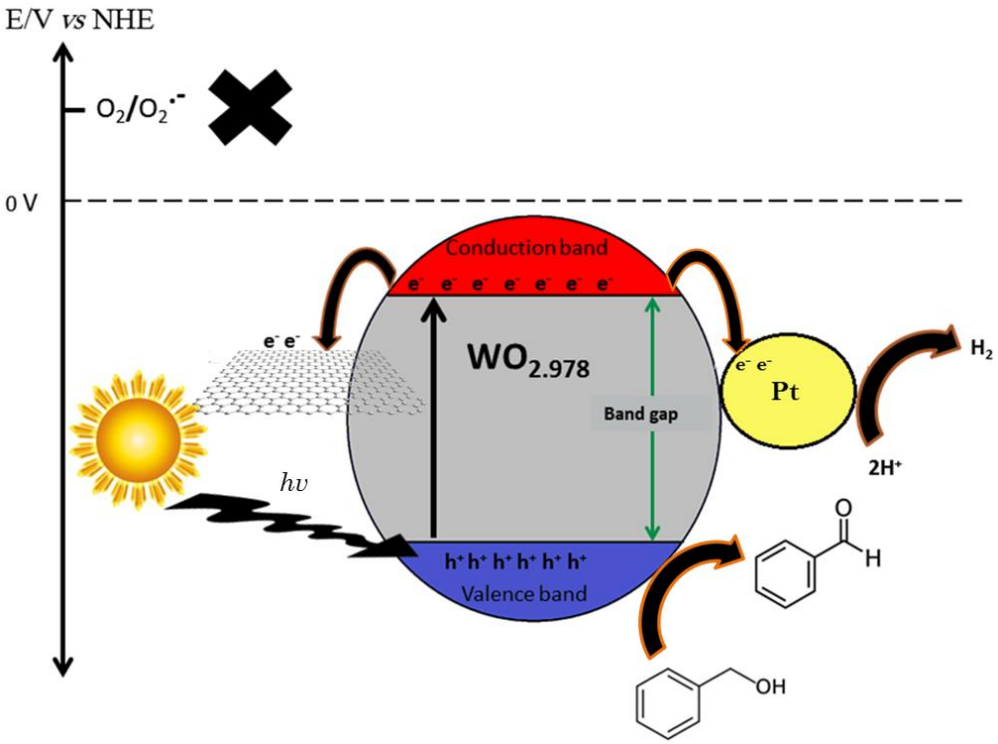

Figure 5.33 : Representation of the reaction mechanism

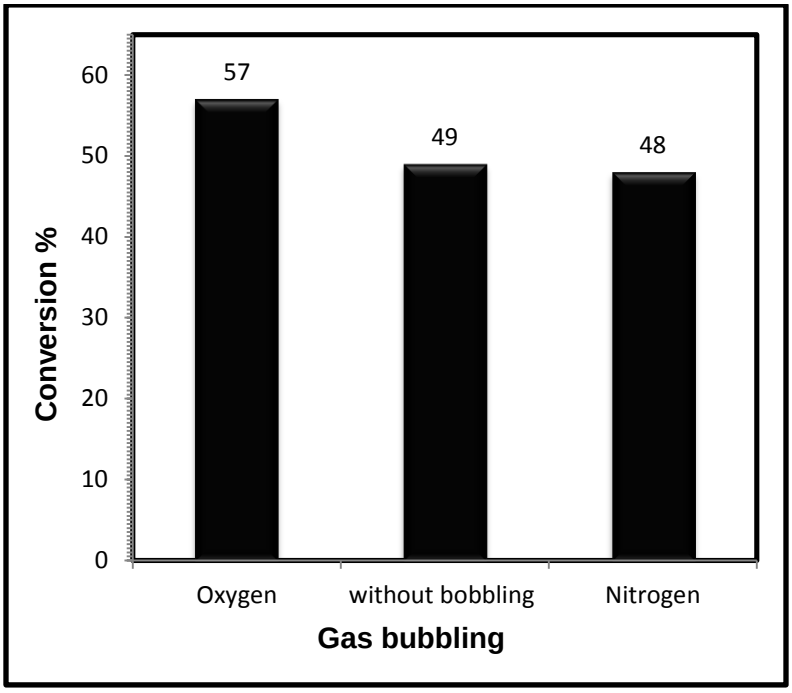

Figure 5.34 : Effect of oxygen bubbling

CHAPTER 6

CONCLUSION AND RECOMMENDATIONS

6.1 Conclusion

Synthesis and characterization of nanostructured tungsten oxide/ graphene composite was investigated. The photocatalytic oxidation of specific alcohols was studied under different concentrations and conditions. The main conclusions from this thesis would include:

- The presence of hydrochloric acid and/or oxalic acid in the hydrothermal synthesis hugely affects the morphology and the size of the synthesized nanostructured tungsten oxide crystals.
- Oxalic acid presence in the hydrothermal preparation significantly increase the surface area of the nanostructured tungsten oxide and hydrochloric acid presence lead to partial reduction of tungsten oxide. However, tungsten oxide prepared in the presence of hydrochloric acid shows better photocatalytic activity than that prepared in the presence of oxalic acid.
- The photocatalytic activity of tungsten oxide toward oxidation of alcohols drastically improved when platinum nanoparticles was deposited on its surface while the improvement is quite well in the case of WO_3/graphene composite.
- Pt/ WO_3/graphene can be used as an alternative and appropriate photocatalyst for the selective oxidation of alcohols in aqueous solutions under simulated sunlight.

6.2 Recommendations:

- Oxidation of different sort of organic compound should be investigated.
- Pt/ WO_3/Gn should be applied on other photocatalytic applications like O_2 and H_2 production.

APPENDIXES

Appendix A: GC-MS running parameter

GC Program

Column Oven Temp. : 50.0 °C
Injection Temp. : 200.00 °C
InjectionMode : Splitless
Sampling Time : 1.00 min
FlowControl Mode : Pressure
Pressure : 14.3 kPa
Total Flow : 5.0 mL/min
Column Flow : 1.50 mL/min
Linear Velocity : 44.4 cm/sec
Purge Flow : 3.0 mL/min
Split Ratio : -1.0
High Pressure Injection : OFF
Carrier Gas Saver : OFF
Fan Starting Temp. : 50.0 °C and less
Oven Temp. Program :

Rate	Temperature(°C)	Hold Time(min)
-	50.0	0.00
10.00	160.0	0.00

External Wait :No
EquilibriumTime :3.0 min

MS program

Micro ScanWidth	:	0.00 amu
IonSourceTemp	:	200.00 °C
Interface Temp.	:	250.00 °C
Solvent Cut Time	:	2.00 min
Detector Gain Mode	:	Relative
Detector Gain	:	+0.20 kV
Start Time	:	2.00 min
End Time	:	11.00 min
ACQMode	:	SIM
Event Time	:	0.30sec

Alcohol	Ch1-m/z	Ch2-m/z
4-methoxybenzyl alcohol	109.00	135.00
Cinnamyl alcohol	115.00	103.00
Benzyl alcohol	108.00	106.00

Appendix B: Detailed BET analysis of WO_3

WO_3-A:

Surface Area:

Single point surface area at p/p° = 0.219654563:	5.8483 m^2/g
BET Surface Area:	1.0678 m^2/g
Langmuir Surface Area:	7.0155 m^2/g
t-Plot Micropore Area:	7.1775 m^2/g
t-Plot External Surface Area:	-6.1097 m^2/g
BJH Adsorption cumulative surface area of pores between 17.000 Å and 3000.000 Å width:	3.896 m^2/g
BJH Desorption cumulative surface area of pores between 17.000 Å and 3000.000 Å width:	5.1760 m^2/g

Pore Volume:

Single point adsorption total pore volume of pores less than 740.961 Å width at p/p° = 0.973168064:	0.018217 cm^3/g
t-Plot micropore volume: 0.005409 cm^3/g	
BJH Adsorption cumulative volume of pores between 17.000 Å and 3000.000 Å width:	0.041595 cm^3/g
BJH Desorption cumulative volume of pores between 17.000 Å and 3000.000 Å width:	0.041595 cm^3/g

Pore Size:

Adsorption average pore width (4V/A by BET):	682.3969 Å
BJH Adsorption average pore width (4V/A):	427.012 Å
BJH Desorption average pore width (4V/A):	321.447 Å

WO_3-B:

Surface Area:

Single point surface area at p/p° = 0.200866391:	42.8682 m^2/g
BET Surface Area:	2.9077 m^2/g
Langmuir Surface Area:	58.3968 m^2/g
t-Plot External Surface Area:	26.1942 m^2/g
BJH Adsorption cumulative surface area of pores between 17.000 Å and 3000.000 Å width:	32.562 m^2/g
BJH Desorption cumulative surface area of pores between 17.000 Å and 3000.000 Å width:	41.3348 m^2/g

Pore Volume:

Single point adsorption total pore volume of pores less than 890.003 Å width at p/p° = 0.977753400:	0.104656 cm^3/g
t-Plot micropore volume:	0.007598 cm^3/g
BJH Adsorption cumulative volume of pores between 17.000 Å and 3000.000 Å width:	0.106940 cm^3/g
BJH Desorption cumulative volume of pores between 17.000 Å and 3000.000 Å width:	0.111408 cm^3/g

Pore Size:

Adsorption average pore width (4V/A by BET):	1439.6834 Å
BJH Adsorption average pore width (4V/A):	131.368 Å
BJH Desorption average pore width (4V/A):	107.810 Å

WO_3-C:

Surface Area:

Single point surface area at p/p° = 0.199758738:	28.2035 m^2/g
BET Surface Area:	29.1484 m^2/g
Langmuir Surface Area:	40.4485 m^2/g
t-Plot Micropore Area:	2.9881 m^2/g
t-Plot External Surface Area:	26.1603 m^2/g
BJH Adsorption cumulative surface area of pores between 17.000 Å and 3000.000 Å width:	29.184 m^2/g
BJH Desorption cumulative surface area of pores between 17.000 Å and 3000.000 Å width:	31.6754 m^2/g

Pore Volume:

Single point adsorption total pore volume of pores less than 768.415 Å width at p/p° = 0.974148604:	0.056385 cm^3/g
t-Plot micropore volume:	0.001086 cm^3/g
BJH Adsorption cumulative volume of pores between 17.000 Å and 3000.000 Å width:	0.061659 cm^3/g
BJH Desorption cumulative volume of pores between 17.000 Å and 3000.000 Å width:	0.061209 cm^3/g

Pore Size:

Adsorption average pore width (4V/A by BET):	77.3769 Å
BJH Adsorption average pore width (4V/A):	84.511 Å
BJH Desorption average pore width (4V/A):	77.296 Å

Appendix C: Detailed PSA analysis of WO_3

WO_3-A:

Summary Data	
MV(um):	115.6
MN(um):	0.657
MA(um):	5.32
CS:	1.128
SD:	116.7
Mz:	109.0
si:	105.2
Ski:	0.372
Kg:	0.707

Percentiles	
%Tile	**Size(um)**
10.00	1.310
20.00	8.25
30.00	29.94
40.00	56.69
50.00	85.96
60.00	126.1
70.00	174.8
80.00	219.0
90.00	269.6
95.00	309.6

Peaks		
Dia(um)	**Vol %**	**Width**
107.0000	88.60	227.1000
0.7870	11.40	0.6680

WO_3-B:

Summary Data	
MV(um):	36.41
MN(um):	0.648
MA(um):	1.170
CS:	5.13
SD:	57.03
Mz:	38.80
si:	59.89
Ski:	0.993
Kg:	9.22

Percentiles	
%Tile	**Size(um)**
10.00	0.580
20.00	0.643
30.00	0.712
40.00	0.814
50.00	1.102
60.00	2.035
70.00	5.50
80.00	51.83
90.00	164.2
95.00	207.6

Peaks		
Dia(um)	**Vol %**	**Width**
151.3000	23.50	166.6000
0.7920	76.50	2.3170

Appendix D: the photocatalysis reactions

Different WO_3:

Bulky WO_3

Time (hours)	Concentration of alcohol mmol/L
0	1
2	1
4	0.99
6	0.99
8	0.99
10	0.99
12	0.99

Nanostructured WO_3-A

Time (hours)	Concentration of alcohol mmol/L
0	1
2	0.98
4	0.97
6	0.97
8	0.96
10	0.96
12	0.95

Nanostructured WO_3-B

Time (hours)	Concentration of alcohol mmol/L
0	1
2	0.99
4	0.99
6	0.99
8	0.98
10	0.98
12	0.98

Nanostructured WO_3-C

Time (hours)	Concentration of alcohol mmol/L
0	1
2	0.98
4	0.97
6	0.97
8	0.96
10	0.96
12	0.96

The absence of irradiation and catalyst:

Nanostructured WO_3-C without the irradiation

Time (hours)	Concentration of alcohol mmol/L
0	1
2	1
4	1
6	1
8	1
10	1
12	1

Irradiation without catalyst

Time (hours)	Concentration of alcohol mmol/L
0	1
2	1
4	1
6	1
8	1
10	1
12	1

Catalyst concentration:

Concentration of the catalyst: 0.5 g/L

Time (hours)	Concentration of alcohol mmol/L
0	1
2	0.94
4	0.91
6	0.89
8	0.87
10	0.86
12	0.85

Concentration of the catalyst: 1 g/L

Time (hours)	Concentration of alcohol mmol/L
0	1
2	0.79
4	0.68
6	0.62
8	0.58
10	0.55
12	0.51

Concentration of the catalyst : 2 g/L

Time (hours)	Concentration of alcohol mmol/L
0	1
2	0.72
4	0.62
6	0.56
8	0.5
10	0.45
12	0.41

Concentration of the catalyst : 3 g/L

Time (hours)	Concentration of alcohol mmol/L
0	1
2	0.7
4	0.55
6	0.46
8	0.4
10	0.35
12	0.31

Alcohol concentration:

Concentration of the alcohol: 0.5 mmol/L

Time (hours)	Concentration of alcohol mmol/L
0	0.5
2	0.43
4	0.39
6	0.36
8	0.33
10	0.3
12	0.28

Concentration of the alcohol: 1 mmol/L

Time (hours)	Concentration of alcohol mmol/L
0	1
2	0.79
4	0.68
6	0.62
8	0.58
10	0.55
12	0.51

Concentration of the alcohol: 1.5 mmol/L

Time (hours)	Concentration of alcohol mmol/L
0	1.5
2	1.04
4	0.75
6	0.53
8	0.42
10	0.37
12	0.33

Concentration of the alcohol: 2 mmol/L

Time (hours)	Concentration of alcohol mmol/L
0	2
2	1.51
4	1.31
6	1.19
8	1.12
10	1.05
12	0.98

Platinum content:

Platinum percentage in Pt/WO_3: 0.5 %

Time (hours)	Concentration of alcohol mmol/L
0	1
2	0.96
4	0.93
6	0.91
8	0.89
10	0.88
12	0.87

Platinum percentage in Pt/WO_3: 1 %

Time (hours)	Concentration of alcohol mmol/L
0	1
2	0.79
4	0.68
6	0.62
8	0.58
10	0.55
12	0.51

Platinum percentage in Pt/WO_3: 1.5 %

Time (hours)	Concentration of alcohol mmol/L
0	1
2	0.75
4	0.63
6	0.54
8	0.47
10	0.42
12	0.39

Platinum percentage in Pt/WO_3: 2 %

Time (hours)	Concentration of alcohol mmol/L
0	1
2	0.74
4	0.61
6	0.52
8	0.44
10	0.39
12	0.35

Platinum percentage in Pt/WO_3: 2.5 %

Time (hours)	Concentration of alcohol mmol/L
0	1
2	0.76
4	0.63
6	0.53
8	0.48
10	0.43
12	0.4

Different alcohols with Pt/WO_3:

4-methoxy benzyl alcohol with Pt/WO_3

Time (hours)	Concentration of alcohol mmol/L
0	1.5
2	1.21
4	0.98
6	0.742
8	0.61
10	0.49
12	0.38

Cinnamyl alcohol with Pt/WO_3

Time (hours)	Concentration of alcohol mmol/L
0	1.5
2	1.12
4	0.84
6	0.64
8	0.492
10	0.36
12	0.238

O_2 and N_2 bubbling:

O_2 bubbling under optima

Time (hours)	Concentration of alcohol mmol/L
0	1
2	0.81
4	0.69
6	0.6
8	0.52
10	0.47
12	0.43

N_2 bubbling under optima

Time (hours)	Concentration of alcohol mmol/L
0	1
2	0.82
4	0.7
6	0.63
8	0.58
10	0.55
12	0.52

Graphene content in WO_3/Gn

Graphene percentage in WO_3/Gn: 0.5 %

Time (hours)	Concentration of alcohol mmol/L
0	1.5
2	1.46
4	1.44
6	1.42
8	1.39
10	1.37
12	1.36

Graphene percentage in WO_3/Gn : 1 %

Time (hours)	Concentration of alcohol mmol/L
0	1.5
2	1.47
4	1.45
6	1.43
8	1.41
10	1.39
12	1.39

Graphene percentage in WO_3/Gn: 2.5 %

Time (hours)	Concentration of alcohol mmol/L
0	1.5
2	1.48
4	1.46
6	1.45
8	1.43
10	1.42
12	1.42

Graphene percentage in WO_3/Gn: 5 %

Time (hours)	Concentration of alcohol mmol/L
0	1.5
2	1.49
4	1.48
6	1.48
8	1.47
10	1.47
12	1.46

Different alcohols with WO_3/Gn nanocomposite:

Benzyl alcohol with WO_3/Gn nanocomposite

Time (hours)	Concentration of alcohol mmol/L
0	1.5
2	1.43
4	1.38
6	1.34
8	1.31
10	1.28
12	1.26

4-methoxy benzyl alcohol with WO_3/Gn nanocomposite

Time (hours)	Concentration of alcohol mmol/L
0	1.5
2	1.46
4	1.43
6	1.41
8	1.39
10	1.38
12	1.38

Cinnamyl alcohol with WO_3/Gn nanocomposite

Time (hours)	Concentration of alcohol mmol/L
0	1.5
2	1.45
4	1.41
6	1.37
8	1.34
10	1.32
12	1.3

Different alcohols with Pt/WO_3/Gn nanocomposite:

Benzyl alcohol with Pt/WO_3/Gn nanocomposite

Time (hours)	Concentration of alcohol mmol/L
0	1.5
2	1.2
4	0.94
6	0.73
8	0.52
10	0.38
12	0.25

4-methoxy benzyl alcohol with Pt/WO_3/Gn nanocomposite

Time (hours)	Concentration of alcohol mmol/L
0	1.5
2	1.11
4	0.75
6	0.55
8	0.41
10	0.35
12	0.29

Cinnamyl alcohol with $Pt/WO_3/Gn$ nanocomposite

Time (hours)	Concentration of alcohol mmol/L
0	1.5
2	1.11
4	0.78
6	0.57
8	0.38
10	0.22
12	0.146

REFERENCES

[1] A.K. Jha, K. Prasad, A. R. Kulkarni. *Coll. Surf. B Biointerfaces.* 71 **2009** 226-229.

[2] E. Ubomba-Jaswa, C. Navntoft, M. I. Polo-Lopez, P. Fernandez-Ibañez, K. G. McGuigan, *Photochem. Photobiol. Sci*., 8 **2009** 587-595.

[3] M.G. Antoniou, J.A. Shoemaker, A.A. de la Cruz, D.D. *Dionysiou, Toxicon* 51 **2008** 1103-1118.

[4] D. Bahnemann, *Photocatalytic water treatment: solar energy applications, Solar Energy*, **2004**, 77, 445–459.

[5] S.L. Liew , Z. Zhang , T.W. Glenn Goh, G.S. Subramanian, H.L. Debbie Seng, T.S. Andy Hor, H.-K. Luo, D.Z. Chi, *Int. J. Hydrogen Energ.*, 39, **2014**, 429-4298.

[6] M.-J. Zhou, N. Zhang, and Z. H. Hou, *Int. J. Photoenergy*, vol. **2014**, Article ID 943537.

[7] J. Sungpanich, T. Thongtem, S. Thongtem. *J. Nanomaterials*, vol. **2014**, Article ID 739251.

[8] A.J. Maira, K.L. Yeung, C.Y. Lee, P.L. Yue, C.K. Chan, *J. Catal.* 192, **2000**, 185.

[9] Z.L. Xu, J. Shang, C.M. Liu, C. Kang, H.C. Guo, Y.G. Du, *Mater. Sci. Eng. B* 63, **1999**, 211.

[10] T. Adschiri, Y. Hakuta, K. Arai, *Ind. Eng. Chem. Res.* **2000**, 39, 4901-4907.

[11] A. N. Lobachev, (ed.), *Crystallization Processes under Hydrothermal Conditions*, pp. 1–255, Consultants Bureau, New York, **1973**.

[12] X. Song, Y. Zhao, Y. Zheng, *Mater. Lett.*60, **2006**, 3405–3408.

[13] X. C. Song, Y. F. Zheng, E. Yang, Y. Wang, *Mater. Lett.*61 ,**2007**, 3904–3908 .

[14] H. G. Choi, Y. H. Jung, D. K. Kim, *J. Am. Ceram. Soc.*, 88 [6] 1684‑1686, **2005**.

[15] J. Wang, E. Khoo, P. S. Lee, J. Ma, *J. Phys. Chem. C* **2009**, 113, 9655–9658.

[16] L. You, Y.F. Sun, J. Ma, Y. Guan, J.M. Sun, Y. Du, G.Y. Lu, *Sens. Actuators B.*157 ,**2011**, 401– 407.

[17] C. Zhao, Y. Yang, Z. Zhang, *J. App. Sci.*, **2012**, 2, 86-92.

[18] N. Zhang, X. Fu, Y. Xu, *J. Mater. Chem*, **2011**, 21, 8152-8158.

[19] M.N. Shaddad, A.M. Al-Mayouf, M.A. Ghanem, M.S. AlHoshan, J.P. Singh, A.A Al-Suhybani, *Int. J. Electrochem. Sci*., 8, **2013**, 2468 – 2478.

[20] C. Wang, L. Yin, L. Zhang, N. Liu, N. Lun, Y. Qi, *ASC Appl. Mater. Interfaces*, **2010**, 2 (11), 3373–3377.

[21] R. Leary, A. Westwood, *Carbon*, 49, **2011**, 741–772.

[22] J. Liu, H. Bai, Y. Wang, Z. Liu, X. Zhang, D.D. Sun, *Adv. Funct. Materials*, 20, **2010**, 4175–4181.

[23] X. An, J.Yu, Y. Wang, Y. Hu, X. Yu, G. Zhang, *J. Mater. Chem*., **2012**, 22, 8525.

[24] K. S. Divya, T. U. Umadevi, S. Mathewa. *J. Nanosci. Lett.* **2014**, 4: 21.

[25] W.S. Hummers Jr., R.E. Offeman, *J. Am. Chem. Soc*. 80 (6), **1958**, 1339.

[26] H.A. Becerril, Mao Jie, Z. Liu, R.M. Stoltenberg, Z. Bao, Y. Chen, *ACS Nano* 2 (3) ,**2008**, 463–470.

[27] S. Chandra, S. Sahu, P. Pramanik, *Mat. Sci. Eng. B.* 167, **2010**, 133–136.

[28] J. Shen, B. Yan, M. Shi, H. Ma, N. Li, M. Ye, *J. Mater. Chem*., **2011**, 21, 3415.

[29] J. Qin, M. Cao, N. Li, C. Hu, *J. Mater. Chem*., **2011**, 21, 17167.

[30] S. Srivastava, K. Jain, V. N. Singh, S. Singh, N Vijayan, N. Dilawar, G. Gupta, T D Senguttuvan, *Nanotechnology*, 23 ,**2012**, 205501.

[31] J. Guo, Y. Li, S. Zhu, Z. Chen, Q. Liu, D. Zhang, W. Moonc, D. Song, *RSC Adv.*, **2012**, 2, 1356–1363.

[32] Y. Zhang, Z. Tang, X. Fu, Y. Xu, *ACS Nano*, **2011**, 5 (9), 7426–7435.

[33] K. Imamura, H. Tsukahara, K. Hamamichi, N. Seto, K. Hashimoto, H. Kominami, *App. Catal. A*, General 450 ,**2013**, 28– 33.

[34] J.C. Collins, W.W. Hess, F.J. Frank. *Tetrahedron Lett.* **1968**, 3363.

[35] E. J. Corey, G. Schmidt, *Tetrahedron Lett*. **1979**, 20, 399.

[36] A. H. Fenselau and J. G. Moffatt, *J. Am. Chem. Soc.* **1963**, 85, 3027.

[37] D. B. Dess, J. C. Martin, *J. Org. Chem.* **1993**, 58, 2899.

[38] de Graauw, C. F.; Peters, J. A.; van Bekkum, H.; Huskens, *J.*,*Synthesis* **1994,** 1007.

[39] U.R. Pillai, E. Sahle-Demessie, *Appl. Catal. A,* 245, **2003**, 103–109.

[40] S.N. Frank, A.J. Bard, *J. Am. Chem. Soc*., **1977**, 99 (1), pp 303–304.

[41] B. Ohtani, O.O. Prieto-Mahaney, D. Li, R. Abe, *J. Photochem. Photobiol . A chem*, 216, **2010,** 179-182.

[42] K.E. Rajashekhar, L.G. Devi, *J. Mol. Catal. A: Chem*. 374–375, **2013**, 12-21.

[43] W. Choi, A. Termin, M.R. Hoffmann, *J. Phys. Chem*. 98, **1994**, 13669-13679.

[44] S. Ahmed, M.G. Rasul, W.N. Martens, R. Brown, M.A. Hashib, *Desalination*, 261, **2010**, 3-18.

[45] T. Hirakawa, Y. Nosaka, *Langmuir,* **2002**, 18, 3247-3254.

[46] S. Yurdakal, G. Palmisano, V. Loddo, V. Augugliaro L. Palmisano, *J. Am. Chem. Soc.* **2008**, 130, 1568-1569.

[47] C.-J. Li, G.-R. Xu, B. Zhang, J. R. Gong, *Appl. Catal. B Environ.* 115– 116, **2012,** 201– 208.

[48] S. Higashimoto, K, Okada, T. Morisugi, M. Azuma, H. Ohue, T.-H. Kim, M. Matsuoka, M. Anpo, *Top Catal.* **2010**, 53:578–583.

[49] S. Higashimoto, R. Shirai, Y. Osano, M. Azuma, H. Ohue, Y. Sakata, H. Kobayashi, *J. Catal.*, 311, **2014**, 137–143.

[50] X. Pan, Y.-J. Xu, *J. Phys. Chem. C*, **2013**, 117, 17996−18005.

[51] N. Zhang, S. Liu, X. Fu, Y.-J. Xu, *J. Phys. Chem. C*, **2011**, 115, 22901–22909.

[52] A. Tanaka, K. Hashimoto, H. Kominami, *J. Am. Chem. Soc.*, **2012**, 134, 14526−14533.

[53] M. Han, B. Özyilmaz, Y. Zhang, P. Kim. *Phys. Rev. Lett*., 98, **2007**, 206805.

[54] K. Kwan, S.W. Cranford. *Chem. Phys. Lett*. 609, **2014**, 65–69.

[55] O. Akhavan, E. Ghaderi. *J. Phys. Chem. C*. 113, **2009**, 20214.

[56] N. Zhang, Y. Zhang, X. Pan, X. Fu, S. Liu, . Y.-J. Xu, *J. Phys. Chem. C*, **2011**, 115, 23501–23511.

[57] M.-Q. Yang, N. Zhang, Y.-J. Xu, *ACS Appl. Mater. Interfaces*, **2013**, 5, 1156−1164.

[58] M. Qamar, M.A. Gondal, Z.H. Yamani *Catal. Commun*. 11, **2010**, 768–772.

[59] S. Chandra, S. Sahu, P. Pramanik, *J. Mat. Sci. Eng. B.* 167, **2010**, 133–136.

[60] S. D. Perera, R. G. Mariano, K. Vu, N. Nour, O. Seitz, Y. Chabal, K. J. Balkus, *ACS Catal.* **2012**, 2, 949−956.

[61] I. M. Szilagyi, B. Forizs, O. Rosseler, A. Szegedi, P. Németh, P. Kiraly, G. Tarkanyi, B. Vajna, K. Varga-Josepovits, K. Laszlo, A. L. Toth, P. Baranyai, M. Leskela, *J. Catal*. 294, **2012**, 119–127.

[62] X. Su, F. Xiao, Y. Li, J. Jian, Q. Sun, J. Wang. *J. Mat. Lett.* 64, **2010**, 1232–1234.

[63] A.P. Shpak, A.M. Korduban, M.M. Medvedskij, V.O. Kandyba, *J. Electron Spectrosc. Relat. Phenom.* 156–158, **2007**, 172–175.

[64] J.C. Dupin, D. Gonbeau, P. Vinatier, A. Levasseur, *Phys*. *Chem. Chem. Phys*. 2, **2000**, 1319.

[65] A. C. Ferrari, J. C. Meyer, V. Scardaci, C. Casiraghi, M. Lazzeri, F. Mauri, S. Piscanec, D. Jiang, K. S. Novoselov, S. Roth, A. K. Geim, *Phys. Rev. Lett.* **2006,** 97, 187401.

[66] A. Gupta, G. Chen, P. Joshi, S. Tadigadapa, P. C. Eklund, *Nano Lett*., **2006**, 6, 2667.

[67] D. Graf, F. Molitor, K. Ensslin, C. Stampfer, A. Jungen, C. Hierold, L. Wirtz, *Nano Lett.*, **2007**, 7, 238.

[68] M. S. Bazarjani, M. Hojamberdiev, K. Morita, G. Zhu, G. Cherkashinin, C. Fasel, T. Herrmann, H. Breitzke, A. Gurlo, R. Riedel, *J. Am. Chem. Soc*. **2013**, 135, 4467−4475.

[69] J. Li, Y. Liu, Z. Zhu, G. Zhang, T. Zou, Z. Zou, S. Zhang, D. Zeng, C. Xie, *Sci. Rep.* 3, 2409; **2013**.

[70] K. Katayama, Y. Takeda, K. Shimaoka, K. Yoshida, R. Shimizu, T. Ishiwata, A. Nakamura, S. Kuwahara, A. Mase, T. Sugita, M. Mori, *Analyst*, **2014**, 139, 1953.

VITAE

Name :Mohamad Omar Alfawakhiry

Nationality :Syrian

Date of Birth :2/28/1988

Email :omarfaw@kfupm.edu.sa , omarfaw88@gmail.com

Address :KFUPM , Dhahran 31932 , Saudi Arabia P.O.Box;8619

Education and Academic Certifications

- Bachelor of "applied chemistry" in 2009, Damascus University, Faculty of Sciences, Chemistry Department with a score of 72.16%.
- Master student in chemistry department at KFUPM with GPA of 3.56.

Work Experience

- Research assistant, chemistry department, faculty of science, Damascus University. From March 2010, till November 2011.
- Research assistant, center of excellence in nanotechnology, Research institute, KFUPM Since November 2011.